Ephemeris Tracking and Error Propagation Analysis of LEO Satellites With Application to Opportunistic Navigation

NADIM KHAIRALLAH
University of Californi, Irvine, CA USA

ZAHER M. KASSAS , Fellow, IEEE
The Ohio State University, Columbus, OH USA

A comprehensive study is performed for low Earth orbit (LEO) space vehicles (SVs) tracking by a receiver opportunistically extracting navigation observables from their downlink radio frequency signals. First, a framework to characterize the LEO SVs orbital motion process noise covariance is developed. Second, the tracking performance via an extended Kalman filter (EKF) is analyzed via comprehensive Monte Carlo simulations for three different sets of observables: 1) pseudorange, 2) Doppler, and 3) fused pseudorange and Doppler measurements. Third, experimental results are presented demonstrating the efficacy of the opportunistic tracking framework in refining the ephemeris of a LEO SV from two-line element (TLE) files. The initial position and velocity errors of over 7.1 km and 7.3 m/s, respectively, of an Orbcomm LEO SV were reduced to 698.7 m and 1.8 m/s, respectively, in just over 6 min of tracking with carrier phase navigation observables, extracted opportunistically. Fourth, the error propagation from the LEO SVs state space to the measurement space and from the measurement space to the receiver's state space is analyzed in the context of stationary receiver localization. Bounds on the magnitude of pseudorange and Doppler residuals are first derived, and the magnitude of the receiver's estimation error is then characterized as a function of errors in the LEO SVs state space. Fifth, experimental results are presented of a stationary receiver tracking an Orbcomm LEO SV by fusing carrier phase observables via an EKF. The tracked LEO ephemeris is then used to localize another stationary receiver, showing a reduction in the receiver's initial horizontal error from 13,476 m to 343 m after just over 6 min. In contrast, it is shown that if the SGP4-propagated ephemeris was used in the EKF to localize the receiver, the error is reduced to 6,852 m, but the filter becomes inconsistent.

I. INTRODUCTION

As of January 2022, over 4000 space vehicles (SVs) were orbiting Earth at altitudes between 160 and 1000 km [1]. This orbital altitude range is referred to as low Earth orbit (LEO) [2] and is the zone where the next space race is currently booming [3], fueled by broadband Internet megaconstellations (e.g., Starlink, Project Kuiper, among others). Currently, SpaceX leads this race with over 2500 Starlink SVs already launched, of which more than 2200 are operational [4]. Furthermore, SpaceX is already approved by the Federal Communications Commission (FCC) to launch over 12 000 SVs and has filed to increase the number of SVs of their Starlink megaconstellation to over 42 000 [5].

This space race, however, can have dire consequences on the sustainability and integrity of space as a shared environment for humanity [6]. With many SVs and space debris already in orbit, a domino effect of space junk generation is likely to happen. This scenario is known as the Kessler syndrome [7] and is named after the NASA astrophysicist who hypothesized it in 1978. The Kessler syndrome states that any collision between space objects would generate numerous pieces of space debris that, in turn, can cause further collisions, thus creating a cascading effect of increasing space debris orbiting Earth. This exponential self-sustaining growth in space junk would pollute space enough that it would render this environment unsustainable for humanity. Space collisions have already happened, the most notable of which being the Iridium 33–Cosmos 2251 collision that occurred in 2009 [8]. The overpopulation of space, particularly in the LEO zone, increases the likelihood of such collisions that would fuel and intensify the effect of the Kessler syndrome [9].

To prevent such a catastrophe, the field of space situational awareness (SSA) was born [10], [11]. SSA aims to keep track of all SVs and space debris orbiting the Earth with the goal of preventing collisions. The current state-of-the-art orbit determination technologies for SSA rely on an array of large telescopes, electro-optical surveillance systems, and radars scattered around the globe as part of the space surveillance network (SSN). Operated by the Combined Space Operations Center, the SSN keeps track of more than 23 000 objects in orbit for SSA purposes [12] using range, angle, and optical measurements from radars, telescopes, and electro-optical surveillance systems.

The LEO SVs ephemeris tracked by the SSN is, however, not released to the public. The most accurate publicly available source to calculate the ephemeris of LEO SVs are

two-line element (TLE) sets published online and updated periodically by the North American Aerospace Defense Command (NORAD) using SSN observations. TLE sets consist of a list of mean orbital elements (inclination angle, right ascension of ascending node, eccentricity, argument of perigee, mean anomaly, and mean motion) and corrective terms given at a specified time epoch [13] that a simplified general perturbation model SGP4 can propagate to a desired inquiry time [14]. Although SGP4 takes into account the variation of the orbital elements due to Earth's oblateness, atmospheric drag, and various short- and long-term perturbations, the TLE-propagated satellite ephemerides suffer from error of a few kilometers in position and a few meters per second in velocity compared to the actual satellite ephemerides.

Despite being launched for communication and broadband Internet [15], LEO SVs present a remarkable potential for both SSA and navigation [16], [17], [18], [19], [20], [21], [22], [23], [24], [25], [26], [27], [28], [29], [30]. On one hand, their signals can be exploited to track LEO satellites, reducing the ephemeris error by orders of magnitude from open-loop propagators (e.g., SGP4) alleviating the need to install expensive radars, telescopes, and electro-optical surveillance systems [31], [32], [33]. On the other hand, LEO SVs offer both geometric and spectral diversities, which are desirable attributes for accurate and resilient navigation, respectively. Moreover, LEO SVs are around twenty times closer to Earth than global navigation satellite systems (GNSS) SVs, which reside in medium Earth orbit (MEO), making LEO signals received with more than 30 dB higher power than their GNSS counterparts [34].

However, there are two main challenges facing opportunistic navigation using LEO SVs. First, their proprietary signals are partially known or completely unknown. For the former case, specialized receivers have been developed, which leverage public knowledge about LEO SVs periodic signals [35], [36], [37], [38], [39]. Even when LEO signals are unknown, cognitive signal processing approaches [40] have been shown to yield useful navigation observables [41], [42]. Second, unlike GNSS SVs, LEO SVs generally do not openly transmit information about their clock error states and ephemeris in their downlink signals. To tackle this challenge, the simultaneous tracking and navigation framework was proposed, in which the receiver estimates its own states simultaneously with the states of the LEO SVs (position, velocity, and clock error) [43]. To deal with the challenge of not knowing the stability of LEO SVs clocks, an interacting multiple-model estimator was developed in [44] to estimate online the clock error states process noise covariance.

Concerning the uncertain LEO SVs ephemerides challenge, SGP4 is the de facto propagator for the publicly available TLE files [45]. However, the magnitude of the LEO SV position error as calculated from the SGP4-propagated TLE ephemeris can range from a few hundred meters to a few kilometers, with most of the error concentrated in the along-track axis of the LEO SVs motion (i.e., along the SVs velocity vector). Beyond SGP4, which is a low-fidelity

analytical propagator that improves computational efficiency at the cost of orbit determination accuracy, semi-analytical and high-fidelity numerical propagators [46] that perform costly numerical integration with complex force models can achieve higher propagation accuracies [47], [48], [49], [50], [51], [52]. However, all numerical and semianalytical propagators require sufficient prior knowledge of various force model parameters (e.g., atmospheric drag, solar radiation pressure, etc.) as well as an accurate initial estimate [53], [54], which are not readily available. Additionally, erroneous model parameters or initial estimates will cause these propagators to diverge due to model mismatches. Recently, machine learning was explored to tackle the orbit determination problem [31], [33], [55], [56], [57], [58], [59], [60]. Although showing great promise, these machine-learning approaches lack formal guarantees of performance.

This article aims to study the tracking of LEO SVs by a receiver opportunistically extracting navigation observables (pseudorange, carrier phase, and/or Doppler) from its radio frequency downlink signals to tackle the uncertain ephemeris challenge. The goal of this study is twofold: 1) offer a framework to track LEO SVs via their navigation observables and 2) enable LEO-based navigation by opportunistically refining publicly available ephemeris information from TLE files, without requiring accurate ephemeris not publicly available. Moreover, the effect of errors in the LEO SVs states on the localization performance of a stationary receiver is analyzed. The contributions of this article are as follows.

1) A methodology to characterize the LEO SVs orbital motion process noise covariance is first presented. Then, a realistic and comprehensive Monte Carlo (MC) simulation study is performed to assess opportunistic LEO SV tracking performance against the open-loop SGP4-propagation of TLEs for three different sets of observables: a) pseudorange, b) Doppler, and c) fused pseudorange and Doppler measurements. These simulations extend [32] by performing MC simulations over various SVs with different elevation profiles with respect to the tracking receiver and with the SGP4 propagator performance evaluated for all realizations.

2) Bounds on the pseudorange and Doppler residuals are derived as a function of LEO SVs ephemeris errors and clocks error states magnitude. Additionally, the magnitude of receiver state estimation error is characterized as a function of the errors in the LEO SVs states. Subsequently, the error propagation from the LEO SVs state space to the measurement space and then to the receiver's state space is analyzed.

3) Experimental results are presented demonstrating the efficacy of the LEO SV tracking framework with a refinement of the Orbcomm FM107 SVs TLE-derived ephemeris from initial position and velocity errors of over 7.1 km and 7.3 m/s down to final errors of 698.7 m and 1.8 m/s, respectively, in just

over 6 min of tracking. Furthermore, the derived bounds on measurement residuals and magnitude of receiver state estimation errors are verified experimentally. The tracked LEO ephemeris is then used to localize another stationary receiver, showing a reduction in the receiver's initial horizontal error from 13,476 m to 343 m. In contrast, it is shown that if the SGP4-propagated ephemeris was used in the EKF to localize the receiver, the error is reduced to 6,852 m, but the filter becomes inconsistent.

The rest of this article is organized as follows. Section II describes the LEO satellites' orbital dynamics and measurement models. Section III discusses the LEO satellite tracking framework and showcases the MC simulation setup and results. Section IV presents derivations of error propagation from the LEO satellites' ephemeris to the measurements and from the measurements to the estimated states. Section V provides experimental results demonstrating the opportunistic tracking of an Orbcomm satellite. Finally, Section VI concludes this article.

II. MODEL DESCRIPTION

This section describes the LEO satellite orbital dynamics and measurement models used in the opportunistic tracking framework.

A. LEO Satellite Dynamics

A two-body model including the most significant nonzero mean perturbing acceleration is adopted as the LEO satellite orbital dynamics model in the Earth-centered inertial (ECI) reference frame. This model offers a tradeoff between accurate open-loop state prediction while maintaining a simple analytical Jacobian for estimation error covariance propagation. The most significant perturbing accelerations for a LEO satellite are due to Earth's nonuniform gravity a_{grav}. The two-body model can be written generally as

$$\ddot{\boldsymbol{r}}_{\text{leo}}(t) = \boldsymbol{a}_{\text{grav}}(t) + \tilde{\boldsymbol{w}}_{\text{leo}}(t), \qquad \boldsymbol{a}_{\text{grav}}(t) = \frac{\partial U(t)}{\partial \boldsymbol{r}_{\text{leo}}(t)} \quad (1)$$

where $\boldsymbol{r}_{\text{leo}} \triangleq [x_{\text{leo}}, y_{\text{leo}}, z_{\text{leo}}]^\mathsf{T}$ is the position vector of the LEO satellite in the ECI frame, U is the nonuniform gravitational potential of Earth at the satellite, and $\tilde{\boldsymbol{w}}_{\text{leo}}$ is a process noise vector in the ECI frame with power spectral density (PSD) $\tilde{\mathbf{Q}}_{\text{leo}}$, which attempts to capture the overall acceleration perturbations including the unmodeled nonuniformity of Earth's gravitational field, atmospheric drag, solar radiation pressure, third-body gravitational forces (e.g., gravity of the Moon and Sun), and general relativity [61].

Several models have been developed for Earth's gravitational potential U. For a satellite requiring accuracies of a few meters, the JGM-3 model developed by Goddard Space Flight Center is usually sufficient [62]. Here, the tesseral and sectoral terms of the JGM-3 model are neglected, since they are several orders of magnitude smaller than the zonal terms

(denoted $\{J_n\}_{n=2}^\infty$). This yields [63]

$$U = \frac{\mu}{\|\boldsymbol{r}_{\text{leo}}\|} \left[1 - \sum_{n=2}^{N} J_n \frac{R_e^n}{\|\boldsymbol{r}_{\text{leo}}\|^n} P_n \left[\sin(\varphi)\right] \right] \quad (2)$$

where μ is Earth's standard gravitational parameter, P_n is a Legendre polynomial with harmonic n, J_n is the nth zonal coefficient, R_e is the mean radius of the Earth, $\sin(\varphi) = z_{\text{leo}}/\|\boldsymbol{r}_{\text{leo}}\|$ (i.e., φ being the LEO SVs latitude), and $N = \infty$. Since the acceleration due to the J_2 coefficient is approximately three orders of magnitude greater than the acceleration due to the other zonal coefficients modeling Earth's oblateness, the perturbation due to nonuniform gravity will be approximated by using only the term corresponding to J_2. Taking the partial derivative of (2) with respect to the components of $\boldsymbol{r}_{\text{leo}}$ with $N \equiv 2$ gives the components of $\boldsymbol{a}_{\text{grav}} \triangleq [\ddot{x}_{\text{grav}}, \ddot{y}_{\text{grav}}, \ddot{z}_{\text{grav}}]^\mathsf{T}$ in the ECI frame as

$$\ddot{x}_{\text{grav}} = -\frac{\mu x_{\text{leo}}}{\|\boldsymbol{r}_{\text{leo}}\|^3} \left[1 + J_2 \frac{3}{2} \left(\frac{R_e}{\|\boldsymbol{r}_{\text{leo}}\|} \right)^2 \left(1 - 5 \frac{z_{\text{leo}}^2}{\|\boldsymbol{r}_{\text{leo}}\|^2} \right) \right]$$

$$\ddot{y}_{\text{grav}} = -\frac{\mu y_{\text{leo}}}{\|\boldsymbol{r}_{\text{leo}}\|^3} \left[1 + J_2 \frac{3}{2} \left(\frac{R_e}{\|\boldsymbol{r}_{\text{leo}}\|} \right)^2 \left(1 - 5 \frac{z_{\text{leo}}^2}{\|\boldsymbol{r}_{\text{leo}}\|^2} \right) \right]$$

$$\ddot{z}_{\text{grav}} = -\frac{\mu z_{\text{leo}}}{\|\boldsymbol{r}_{\text{leo}}\|^3} \left[1 + J_2 \frac{3}{2} \left(\frac{R_e}{\|\boldsymbol{r}_{\text{leo}}\|} \right)^2 \left(3 - 5 \frac{z_{\text{leo}}^2}{\|\boldsymbol{r}_{\text{leo}}\|^2} \right) \right]. \quad (3)$$

B. Clock Dynamics Model

The receiver's and LEO SVs clock error state dynamics are assumed to evolve in discrete-time according to [64]

$$\boldsymbol{x}_{\text{clk},i}(k+1) = \mathbf{F}_{\text{clk}} \boldsymbol{x}_{\text{clk},i}(k) + \boldsymbol{w}_{\text{clk},i}(k)$$

$$\boldsymbol{x}_{\text{clk},i} \triangleq \begin{bmatrix} c\delta t_i, & c\dot{\delta} t_i \end{bmatrix}^\mathsf{T}, \quad \mathbf{F}_{\text{clk}} = \begin{bmatrix} 1 & T \\ 0 & 1 \end{bmatrix} \quad (4)$$

where $i = \{r, \text{leo}\}$, δt_i is the clock bias, $\dot{\delta} t_i$ is the clock drift, c is the speed of light, T is the constant sampling interval, and $\boldsymbol{w}_{\text{clk},i}$ is the process noise, which is modeled as a discrete-time white noise sequence with covariance

$$\mathbf{Q}_{\text{clk},i} = c^2 \cdot \begin{bmatrix} S_{\tilde{w}_{\delta t_i}}T + S_{\tilde{w}_{\dot{\delta} t_i}}T^3/3 & S_{\tilde{w}_{\dot{\delta} t_i}}T^2/2 \\ S_{\tilde{w}_{\dot{\delta} t_i}}T^2/2 & S_{\tilde{w}_{\dot{\delta} t_i}}T \end{bmatrix}. \quad (5)$$

The terms $S_{\tilde{w}_{\delta t_i}}$ and $S_{\tilde{w}_{\dot{\delta} t_i}}$ are the clock bias and drift process noise PSDs, respectively, which can be related to the power-law coefficients, $\{h_{\alpha_i}\}_{\alpha_i=-2}^2$, which have been shown through laboratory experiments to characterize the PSD of the fractional frequency deviation of an oscillator from nominal frequency according to $S_{\tilde{w}_{\delta t_i}} \approx \frac{h_{0,i}}{2}$ and $S_{\tilde{w}_{\dot{\delta} t_i}} \approx 2\pi^2 h_{-2,i}$ [65]. The receiver's and LEO SVs process noise covariances $\mathbf{Q}_{\text{clk},r}$ and $\mathbf{Q}_{\text{clk,leo}}$ are calculated from (5) using the PSDs associated with the receiver's and LEO SVs oscillator quality, respectively.

C. Pseudorange Measurement Model

A LEO receiver extracts pseudorange measurements ρ from LEO SVs by estimating the time of arrival. The pseudorange ρ from the LEO SV to the receiver at time-step

k, which represents discrete-time instant $t_k = kT + t_0$ for an initial time t_0, is modeled as

$$\rho(k) = \left\| \boldsymbol{r}_r(k) - \boldsymbol{r}_{\text{leo}}(k') \right\|_2 + c \cdot \left[\delta t_r(k) - \delta t_{\text{leo}}(k') \right]$$
$$+ c\delta t_{\text{iono}}(k) + c\delta t_{\text{tropo}}(k) + v_\rho(k) \quad (6)$$

where k' represents discrete time at $t_{k'} = kT + t_0 - \delta t_{\text{TOF}}$, with δt_{TOF} being the true time-of-flight of the signal from the LEO SV to the receiver; $\boldsymbol{r}_r$ and $\boldsymbol{r}_{\text{leo}}$ are the receiver's and LEO SVs 3-D position vectors expressed in the same reference frame, respectively; c is the speed of light; δt_r and δt_{leo} are the receiver's and LEO SV transmitter's clock biases, respectively; δt_{iono} and δt_{tropo} are the ionospheric and tropospheric delays affecting the LEO SVs signal, respectively; and $v_\rho(k)$ is the pseudorange measurement noise, which is modeled as a zero-mean white Gaussian random sequence with variance $\sigma_\rho^2(k)$.

D. Doppler Measurement Model

A LEO receiver extracts Doppler frequency measurements f_D from LEO satellites by subtracting the nominal carrier frequency from the received signal frequency. A pseudorange rate measurement $\dot{\rho}$ can be obtained from

$$\dot{\rho}(t) = -\frac{c}{f_c} f_D(t) \quad (7)$$

where f_c is the carrier frequency.

The pseudorange rate measurement $\dot{\rho}$ from the LEO SV to the receiver at time-step k can be modeled as

$$\dot{\rho}(k) = \left[\dot{\boldsymbol{r}}_r(k) - \dot{\boldsymbol{r}}_{\text{leo}}(k') \right]^\mathsf{T} \frac{\left[\boldsymbol{r}_r(k) - \boldsymbol{r}_{\text{leo}_l}(k') \right]}{\left\| \boldsymbol{r}_r(k) - \boldsymbol{r}_{\text{leo}}(k') \right\|_2}$$
$$+ c \cdot \left[\dot{\delta t}_r(k) - \dot{\delta t}_{\text{leo}}(k') \right] + c\dot{\delta t}_{\text{iono}}(k)$$
$$+ c\dot{\delta t}_{\text{tropo}}(k) + v_{\dot{\rho}}(k) \quad (8)$$

where $\dot{\boldsymbol{r}}_r$ and $\dot{\boldsymbol{r}}_{\text{leo}}$ are the receiver's and LEO SVs 3-D velocity vectors expressed in the same reference frame, respectively; $\dot{\delta t}_r$ and $\dot{\delta t}_{\text{leo}}$ are the receiver's and LEO SVs transmitter clock drifts, respectively; $\dot{\delta t}_{\text{iono}}$ and $\dot{\delta t}_{\text{tropo}}$ are the ionospheric and tropospheric delay rates affecting the LEO SVs signal, respectively; and $v_{\dot{\rho}}(k)$ is the pseudorange rate measurement noise, which is modeled as a zero-mean white Gaussian random sequence with variance $\sigma_{\dot{\rho}}^2(k)$.

E. Carrier Phase Measurement Model

The continuous-time carrier phase observable can be obtained by integrating the Doppler measurement over time [66]. The carrier phase measurement ϕ (expressed in meters) made by the receiver on the LEO SV at time-step k can be modeled in discrete time as

$$\phi(k) = \left\| \boldsymbol{r}_r(k) - \boldsymbol{r}_{\text{leo}}(k') \right\|_2 + c \cdot \left[\delta t_r(k) - \delta t_{\text{leo}}(k') \right] + \lambda N$$
$$+ c\delta t_{\text{iono}}(k) + c\delta t_{\text{tropo}}(k) + v_\phi(k) \quad (9)$$

where λ is the wavelength of the carrier signal transmitted by the LEO SV, N is the carrier phase ambiguity of the LEO SV carrier phase measurement, and $v_\phi(k)$ is the measurement noise, which is modeled as a zero-mean white Gaussian random sequence with variance $\sigma_\phi^2(k)$.

III. OPPORTUNISTIC LEO SATELLITE TRACKING

This section formulates the LEO SV tracking framework and presents simulation results comparing the tracking performance with pseudorange, Doppler, and fused pseudorange and Doppler versus SGP4s open-loop propagation.

A. Tracking Filter Formulation

An extended Kalman filter (EKF) is implemented to perform the tracking of LEO SVs by a receiver opportunistically extracting navigation observables from the satellite's downlink signals. The state vector estimated by the EKF is defined as

$$\boldsymbol{x} \triangleq \left[\boldsymbol{x}_{\text{leo}}^\mathsf{T}, \boldsymbol{x}_{\text{clk}}^\mathsf{T} \right]^\mathsf{T}, \quad \boldsymbol{x}_{\text{leo}} \triangleq \left[\boldsymbol{r}_{\text{leo}}^\mathsf{T}, \dot{\boldsymbol{r}}_{\text{leo}}^\mathsf{T} \right]$$
$$\boldsymbol{x}_{\text{clk}} \triangleq \left[c \cdot (\delta t_r - \delta t_{\text{leo}}) , c \cdot (\dot{\delta t}_r - \dot{\delta t}_{\text{leo}}) \right]^\mathsf{T}$$

where $\boldsymbol{r}_{\text{leo}}$ and $\dot{\boldsymbol{r}}_{\text{leo}}$ are the LEO SVs 3-D position and velocity vectors, expressed in the ECI reference frame, respectively.

The propagation of the LEO SVs position $\boldsymbol{r}_{\text{leo}}$ and velocity $\dot{\boldsymbol{r}}_{\text{leo}}$ is performed by numerical integration of the orbital dynamics equations of motion in (3) during the prediction step of the EKF.

B. LEO Orbital Motion Process Noise Characterization

Since the process noise covariance matrix $\mathbf{Q}_{\boldsymbol{r}\dot{\boldsymbol{r}}_{\text{leo}}}$ of the LEO SVs orbital motion (position and velocity states) not only affects the uncertainty propagation, but also the states' estimates in the tracking filter, it is critical to accurately characterize $\mathbf{Q}_{\boldsymbol{r}\dot{\boldsymbol{r}}_{\text{leo}}}$. To this end, the following general MC-based methodology is adopted.

1) A NORAD-generated publicly available TLE reference file is selected for a LEO SV. The reference TLE epoch as well as the six mean Keplerian elements and corrective terms given at this TLE epoch fully define the orbit of the Orbcomm SV. This reference TLE is propagated for a duration of K seconds spanning just over one orbital period (e.g., $K = 6000$ for Orbcomm), with a time step of 1 s using the SGP4 propagator. The predicted SV position and velocity are saved in $\boldsymbol{x}_{\boldsymbol{r}\dot{\boldsymbol{r}},\text{ref}}(k)$, $k = 1, 2, \ldots, K+1$.

2) N MC realizations are generated by drawing samples from a Gaussian distribution centered at the reference TLE mean Keplerian elements. For each of these N realizations, a TLE file is generated with the same epoch and corrective terms as the reference TLE but with the randomized mean Keplerian elements.

3) Each of the N randomized TLE realizations of the reference TLE are propagated for K seconds with a time step of 1 s using the SGP4 propagator and the predicted SV position and velocity $\boldsymbol{x}_{\boldsymbol{r}\dot{\boldsymbol{r}}, j}(k)$ are stored at each time-step k for each realization j, where $k = 1, 2, \ldots, K+1$ and $j = 1, 2, \ldots, N$.

4) For each realization j, the value of the process noise $\boldsymbol{w}_{\boldsymbol{r}\dot{\boldsymbol{r}}, j}$ is calculated at each time-step $k = 1, \ldots, K$ according to $\boldsymbol{w}_{\boldsymbol{r}\dot{\boldsymbol{r}}, j}(k) = \boldsymbol{x}_{\boldsymbol{r}\dot{\boldsymbol{r}}, j}(k+1) - \boldsymbol{f}_{\boldsymbol{r}\dot{\boldsymbol{r}}}[\boldsymbol{x}_{\boldsymbol{r}\dot{\boldsymbol{r}}, j}(k)]$,

where $f_{r\dot{r}}$ is the nonlinear dynamics model used in the filter's prediction step to propagate the SVs position and velocity states. In this article, $f_{r\dot{r}}$ is specifically taken to be such that $f_{r\dot{r}}(r) = \dot{r}$ and $f_{r\dot{r}}(\dot{r}) = \ddot{r}$, where $\ddot{r}$ are described by the two-body with J2 perturbations equations of motion in (3).

5) The empirical covariance $\mathbf{Q}_{r\dot{r},\text{emp}}$ of the process noise is computed at each time-step k by averaging $w_{r\dot{r},j}(k)w_{r\dot{r},j}^\top(k)$ across MC realizations according to $\mathbf{Q}_{r\dot{r},\text{emp}}(k) = \frac{1}{N}\sum_{j=1}^{N} w_{r\dot{r},j}(k)w_{r\dot{r},j}^\top(k)$, $k = 1, \ldots, K$.

Since both the SGP4 propagation $x_{r\dot{r},j}(k+1)$ and the filter's prediction $f_{r\dot{r}}[x_{r\dot{r},j}(k)]$ are performed in the ECI reference frame, the process noise vectors $w_{r\dot{r},j}(k)$ are also expressed in the ECI frame. As a result, $\mathbf{Q}_{r\dot{r},\text{emp}}(k)$ will be the empirical process noise covariance at each time-step expressed in the ECI frame.

To provide an intuitive interpretation of the effect of the process noise on the LEO SVs motion, the rotation matrix $\mathbf{R}_i^o$ from the ECI frame, denoted $\{i\}$, to the SVs radial–transverse–normal (RTN) frame, denoted $\{o\}$ for an orbital frame, where the transverse and normal axes correspond to along-track and cross-track directions, respectively, is computed at each time-step k. The empirical process noise covariance determined by the MC analysis described above $^i\mathbf{Q}_{r\dot{r},\text{emp}}(k)$ is then rotated to form $^o\mathbf{Q}_{r\dot{r},\text{emp}}(k)$, $k = 1, 2, \ldots, K$.

In addition, $^o\mathbf{Q}_{r\dot{r},\text{emp}}$ is more invariant than $^i\mathbf{Q}_{r\dot{r},\text{emp}}$ since in the SVs RTN frame, the SVs motion is constrained to be in the along-track–radial plane (orbital plane) with the velocity in the along-track direction and with no motion in the cross-track direction; whereas in the ECI frame, the LEO SVs motion has generally components in all directions, which are time varying as the SV orbits Earth. Moreover, the invariance brought by the expression of the process noise covariance matrix in the SVs RTN frame allows for a generalization of $^o\mathbf{Q}_{r\dot{r},\text{emp}}$ to all LEO SVs, which have similar motion characteristics in the RTN frame, while $^i\mathbf{Q}_{r\dot{r},\text{emp}}$ would only be applicable for the reference SV chosen in the MC framework at a specific time determined by the SVs position in the ECI frame. To further enhance the generalization of the process noise covariance matrix, the invariance of $^o\mathbf{Q}_{r\dot{r},\text{emp}}$ is leveraged to define $^o\bar{\mathbf{Q}}_{r\dot{r},\text{emp}} \triangleq \frac{1}{K}\sum_{k=1}^{K} {^o\mathbf{Q}_{r\dot{r},\text{emp}}}(k)$, which will be used in the LEO SV tracking filter. The 95th-percentile error ellipsoid associated with the LEO SVs position states (i.e., top-left 3×3 block of $^o\bar{\mathbf{Q}}_{r\dot{r},\text{emp}}$) can be visualized in Fig. 1.

To validate this methodology, the empirical position and velocity covariance matrix $^i\mathbf{P}_{r\dot{r},\text{emp}}(k) = \frac{1}{N}\sum_{j=1}^{N} \tilde{x}_{r\dot{r},j}(k)\tilde{x}_{r\dot{r},j}^\top(k)$, where $\tilde{x}_{r\dot{r},j}(k) \triangleq x_{r\dot{r},\text{ref}}(k) - x_{r\dot{r},j}(k)$, is computed from $N = 100$ MC runs of SGP4 propagation of different TLE realizations. In parallel, the filter's open-loop formal covariance is computed by propagating the *initial* empirical position and velocity covariance matrix $^i\mathbf{P}_{r\dot{r},\text{emp}}(1)$ via the nonlinear dynamics $f_{r\dot{r}}$ coupled to the $^o\bar{\mathbf{Q}}_{r\dot{r},\text{emp}}$ term to account for the process

$$\mathbf{R}_i^o = \begin{bmatrix} \bar{x}_i \cdot \bar{x}_o & \bar{y}_i \cdot \bar{x}_o & \bar{z}_i \cdot \bar{x}_o \\ \bar{x}_i \cdot \bar{y}_o & \bar{y}_i \cdot \bar{y}_o & \bar{z}_i \cdot \bar{y}_o \\ \bar{x}_i \cdot \bar{z}_o & \bar{y}_i \cdot \bar{z}_o & \bar{z}_i \cdot \bar{z}_o \end{bmatrix}$$
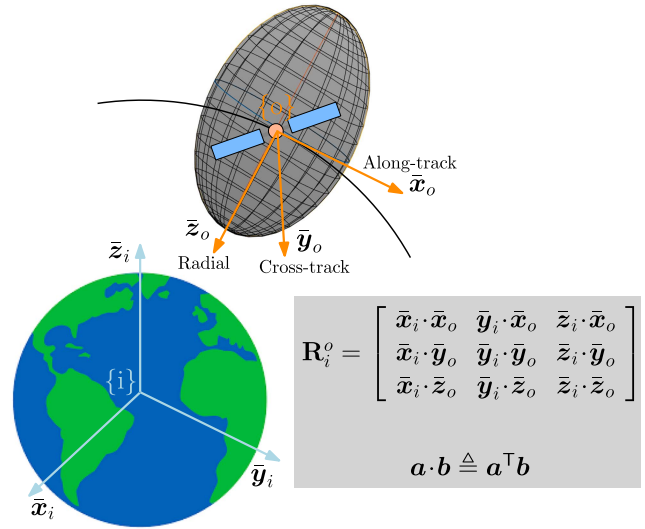
$$a \cdot b \triangleq a^\top b$$

Fig. 1. Visualization of the 95th-percentile error ellipsoid of the averaged process noise covariance characterized for one orbital period for the LEO SV's position states. The rotation matrix $\mathbf{R}_i^o$ rotates the coordinates of a vector expressed in the ECI frame $\{i\}$ into the LEO SV's RTN frame $\{o\}$. The principal directions of $\{i\}$ and $\{o\}$ are represented by the unit vectors $\bar{x}_i, \bar{y}_i, \bar{z}_i$ and $\bar{x}_o, \bar{y}_o, \bar{z}_o$, respectively. The notation $a \cdot b$ denotes the inner product of vectors a and b.
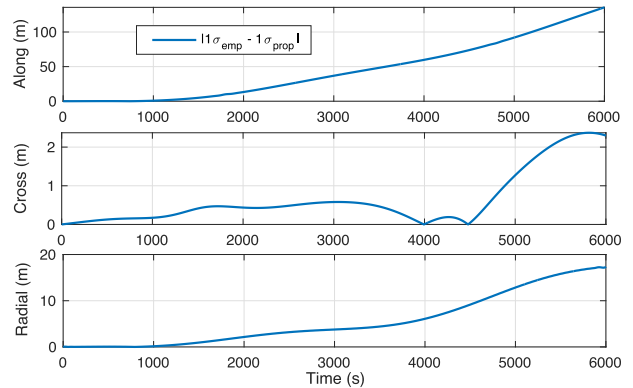

Fig. 2. Absolute difference between the empirical and propagated formal position standard deviations in the RTN frame for one orbital period.

noise of the SVs position and velocity states and is denoted by $^i\mathbf{P}_{r\dot{r},\text{prop}}(k)$. At each time-step k, $^o\bar{\mathbf{Q}}_{r\dot{r},\text{emp}}$ was rotated using the current rotation matrix $\mathbf{R}_o^i(k)$ to form $^i\bar{\mathbf{Q}}_{r\dot{r},\text{emp}}(k)$ and perform the propagation of $^i\mathbf{P}_{r\dot{r},\text{prop}}$ in the ECI frame. Finally, the absolute difference between the empirical and propagated position standard deviations is plotted in Fig. 2 in the LEO SVs RTN frame for $k = 1, \ldots, K+1$.

The following comments and observations can be made. First, although the difference between the SGP4-propagated ephemerides and the orbital dynamics model $f_{r\dot{r}}$ used is deterministic, the randomness in this approach stems from the initial dispersion of TLEs around the reference TLE in step 2 of the above methodology. Second, SGP4 was chosen as the source of the truth orbit model since using a higher-fidelity analytical propagator would result in a less representative ephemeris without accurate knowledge of the
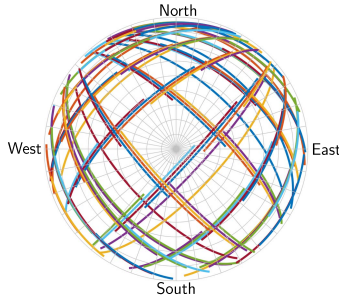
Fig. 3. Skyplot of simulated trajectories of 103 SVs.

ballistic coefficient [53], [54], which is not readily available. Third, the deviation of the SGP4 predictions from the actual truth ephemeris is small for 1-s propagation intervals and justifies the use of SGP4 as the source of orbit truth in this analysis. Fourth, the error ellipsoid of the LEO SVs position states process noise covariance matrix is mostly elongated in the radial direction (see Fig. 1). This can be explained by the fact that most of the acceleration perturbations are in this direction and are mainly caused by the unmodeled nonuniformity of Earth's gravitational potential beyond the J_2 term. Fifth, the absolute difference between the empirical and propagated LEO SV position states standard deviations is the largest for the along-track axis, revealing that the LEO SV position process noise covariance was matched the least in this direction. Nevertheless, the absolute difference for the position in the along-track axis is less than 150 m after more than one orbit of open-loop propagation around Earth, as shown in Fig. 2. For time spans less than 10 min, during which a LEO SV is typically visible to a receiver, this absolute difference is very small. Finally, the close agreement between the empirical and formal covariances in Fig. 2 demonstrates that the orbital motion process noise covariance characterized by the averaging approach in the above methodology is reliable to be used in the tracking filter.

C. Simulation Setup

A comprehensive MC simulation is performed to study the efficacy of opportunistic LEO SV tracking using three different sets of observables: 1) pseudorange measurements, 2) Doppler measurements, and 3) fused pseudorange and Doppler measurements. In this simulation, 103 SVs with diverse elevation profiles and geometries relative to the receiver, as depicted in the skyplot in Fig. 3, are tracked with each set of measurements at a rate of 1 Hz for a duration of 5 min. For each of the 103 SVs, 100 MC runs are simulated resulting in a total of 10 300 tracking runs for each set of observables. In each MC run, the initial SVs position and velocity are obtained from a randomized TLE, which is generated with realistic errors consistent with uncertainties observed in NORAD-published TLEs. Moreover, the time evolution of the receiver's and LEO SVs clock error states as well as the measurement noise are randomized for each MC run. The simulation setup and randomization settings are presented next.

TABLE I
Receiver's and LEO SVs' Oscillator Parameters

Quality	Coefficients $\{h_0, h_{-2}\}$
Receiver's typical-quality OCXO	$\{8.0 \times 10^{-20}, 4.0 \times 10^{-23}\}$
LEO SVs' high-quality OCXO	$\{2.6 \times 10^{-22}, 4.0 \times 10^{-26}\}$

1) *Receiver and LEO Satellites' Trajectories:* The tracking receiver was simulated to be stationary with a known location on the University of California, Irvine, USA campus. The receiver was placed on the top of a parking structure to guarantee an open sky environment with no obstructed views in all directions. Consequently, multipath effects affecting the incoming SV downlink signals are assumed to be negligible for the tracking receiver. Also, since the LEO SV tracking is performed in the ECI frame, the receiver's position and velocity is also found in the ECI frame by converting the stationary Earth-centered, Earth-fixed (ECEF) position while accounting for Earth's rotation, nutation and precession effects, and polar motion.

The FCC-approved 12 000-satellite Starlink LEO constellation was simulated using orbital parameters found in the FCC filings. The LEO SV trajectories were obtained through SGP4 propagations of simulated TLEs for the Starlink satellite megaconstellation. The elevation angle mask was set to $10°$.

2) *Clock Errors:* The receiver was assumed to be equipped with a typical-quality oven-controlled crystal oscillator (OCXO) and the LEO SVs were assumed to have high-quality OCXOs. The power-law coefficients of these oscillators are given in Table I and can be used to compute the discrete-time process noise covariance for the clock error states $\mathbf{Q}_{\text{clk},r}$ and $\mathbf{Q}_{\text{clk,leo}}$. The clock bias and drift of the LEO receiver and LEO SV transmitters were simulated according to the standard two-state clock error model [64]. The values of the receiver's clock error states $\boldsymbol{x}_{\text{clk},r}(0) \triangleq [c\delta t_r(0), c\dot{\delta} t_r(0)]$ were initialized as $\boldsymbol{x}_{\text{clk},r}(0) \sim \mathcal{N}[\mathbf{0}_{2\times1}, \mathbf{P}_{\text{clk},r}]$, where $\mathbf{P}_{\text{clk},r} = \text{diag}[9 \times 10^4, 9 \times 10^{-2}]$ with units of $[\text{m}^2, (\text{m/s})^2]$ corresponding to a 1σ of 1 μs and 1 ns/s for the clock bias and drift, respectively. The values of the LEO SVs clock error states $\boldsymbol{x}_{\text{clk,leo}}(0) \triangleq [c\delta t_{\text{leo}}(0), c\dot{\delta} t_{\text{leo}}(0)]$ were initialized as $\boldsymbol{x}_{\text{clk,leo}}(0) \sim \mathcal{N}[\mathbf{0}_{2\times1}, \mathbf{P}_{\text{clk,leo}}]$, where $\mathbf{P}_{\text{clk,leo}} = \text{diag}[9 \times 10^2, 9 \times 10^{-4}]$ with units of $[\text{m}^2, (\text{m/s})^2]$ corresponding to a 1σ of 0.1 μs and 0.1 ns/s for the clock bias and drift, respectively.

3) *Measurements:* Pseudorange navigation observables to all visible LEO SVs were generated according to (6). The time-varying pseudorange measurement noise variances were calculated from the predicted carrier-to-noise (C/N_0), which was found from the log-distance path loss model

$$(C/N_0)_l(k) = P_0 - 10\log_{10}(d_l(k)/D_0) \qquad (10)$$

where $P_0 = 56$ dB-Hz is the nominal C/N_0 at a distance $D_0 = 1000$ km and $d_l(k) \triangleq \|\boldsymbol{r}_r(k) - \boldsymbol{r}_{\text{leo}_l}(k)\|_2$ is the distance between the receiver and the lth LEO SV. The pseudorange measurement noise variances are proportional

to the square root of the inverse of C/N_0, expressed in linear units, and ranged between 0.43 and 3.73 m^2.

Pseudorange rate measurements to all visible LEO SVs were generated according to (8). Pseudorange rate measurements are directly proportional to Doppler frequency observables as demonstrated in (7) but are independent of the carrier frequency. Hence, pseudorange rate measurements were preferred over Doppler to obtain comparable measurements from different constellations, which transmit downlink signals at frequencies that are orders of magnitude apart. From (10), based on the distance between the receiver and SVs, the pseudorange rate measurement noise variances, expressed in linear units, ranged between 0.13 and 1.17 (m/s)^2.

The simulated measurements were assumed to have been corrected for tropospheric and ionospheric effects using available models in the literature [66]. The remaining modeling errors are lumped in the white measurement noise, with temporal correlations being neglected for simplicity. Future studies could readily generalize these simulations by incorporating such correlations.

D. Filter Initialization

The lth LEO SV position and velocity state estimates $\hat{x}_{r\dot{r}_{\text{leo},l}}(0|0) \triangleq [\hat{r}_{\text{leo},l}^{\mathsf{T}}(0|0), \hat{\dot{r}}_{\text{leo},l}^{\mathsf{T}}(0|0)]^{\mathsf{T}}$ were initialized in the ECI frame, denoted by $\{i\}$, as follows:

$$\hat{x}_{r\dot{r}_{\text{leo},l}}(0|0) \sim \mathcal{N}\left[x_{r\dot{r}_{\text{leo},l}}(0),\ \mathbf{P}_{x_{r\dot{r}_{\text{leo},l}}}(0|0)\right]$$

$$\mathbf{P}_{x_{r\dot{r}_{\text{leo},l}}}(0|0) \triangleq \text{diag}\left[\mathbf{P}_{x_{r_{\text{leo},l}}}(0|0),\ \mathbf{P}_{x_{\dot{r}_{\text{leo},l}}}(0|0)\right]$$

$$\mathbf{P}_{x_{r_{\text{leo},l}}}(0|0) = \mathbf{R}_{o_{\text{leo},l}}^{i}(0)^{o_{\text{leo}}}\mathbf{P}_{x_{r_{\text{leo}}}}(0|0)\left[\mathbf{R}_{o_{\text{leo},l}}^{i}(0)\right]^{\mathsf{T}}$$

$$\mathbf{P}_{x_{\dot{r}_{\text{leo},l}}}(0|0) = \mathbf{R}_{o_{\text{leo},l}}^{i}(0)^{o_{\text{leo}}}\mathbf{P}_{x_{\dot{r}_{\text{leo}}}}(0|0)\left[\mathbf{R}_{o_{\text{leo},l}}^{i}(0)\right]^{\mathsf{T}}$$

where $x_{r\dot{r}_{\text{leo},l}}(0)$ is the lth LEO SVs true position and velocity states in ECI and $\mathbf{P}_{x_{r\dot{r}_{\text{leo},l}}}(0|0)$ is the associated initial covariance; $^{o_{\text{leo}}}\mathbf{P}_{x_{r_{\text{leo}}}}(0|0) \triangleq \text{diag}[4 \times 10^6, 10^2, 10^4]$ m^2 and $^{o_{\text{leo}}}\mathbf{P}_{x_{\dot{r}_{\text{leo}}}}(0|0) \triangleq \text{diag}[4 \times 10^{-2}, 10^{-4}, 4]$ (m/s)^2 are the initial LEO SVs position and velocity covariances in the SVs orbital RTN frame $\{o_{\text{leo}}\}$, respectively; and $\mathbf{R}_{o_{\text{leo},l}}^{i}(0)$ is the initial rotation matrix from the l th LEO SVs orbital RTN frame $\{o_{\text{leo}_l}\}$ to the ECI frame $\{i\}$. The first entry of the LEO SVs position and velocity covariances in the SVs RTN frame corresponds to the SVs along-track axis, the second entry is associated with the cross-track direction, and the last entry is for the radial axis. These values were carefully selected to closely match the uncertainties inherent to TLE files with the most uncertainty being in the along-track position and radial velocity while the cross-track direction TLE errors are the least substantial as the SVs motion is constrained in the orbital (along-track–radial) plane.

The LEO SVs position and velocity states process noise covariance $^o\bar{\mathbf{Q}}_{r\dot{r},\text{emp}}$ found from the methodology in Section III-B was used in the EKF to account for the effect of unmodeled uncertainties in the LEO SVs orbital motion. This process noise covariance matrix expressed in the SVs RTN frame was rotated to the ECI frame at each EKF time
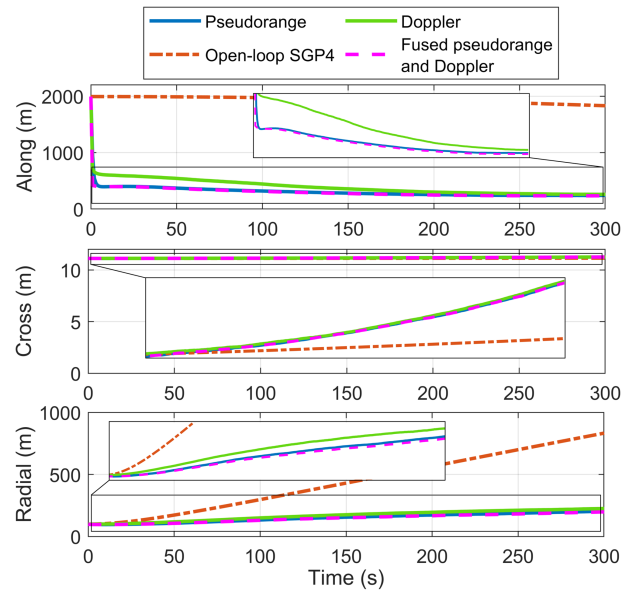

Fig. 4. Position RMSEs for tracking using pseudorange, Doppler, and fused pseudorange and Doppler versus SGP4's open-loop position RMSE.

update step for every LEO SV. Note that the time-step of 1 s, chosen in Section III-B, is consistent with the propagation time-step in the EKF, as the measurement updates are performed at a rate of 1 Hz.

The filter's clock error states $x_{\text{clk}}(0|0)$ were initialized as $x_{\text{clk}}(0|0) \sim \mathcal{N}[\mathbf{0}_{2\times1},\ \mathbf{P}_{\text{clk}}(0|0)]$, where $\mathbf{P}_{\text{clk}}(0|0) = \mathbf{P}_{\text{clk},r} + \mathbf{P}_{\text{clk},\text{leo}}$. The process noise covariance for the filter's clock error states is set to $\mathbf{Q}_{\text{clk}} = \mathbf{Q}_{\text{clk},r} + \mathbf{Q}_{\text{clk},\text{leo}}$, with $\mathbf{Q}_{\text{clk},r}$ and $\mathbf{Q}_{\text{clk},\text{leo}}$ computed from (5) using the oscillator parameters found in Table I.

E. Tracking Results

This section presents MC tracking simulation results for the three observable sets: 1) pseudorange measurements, 2) Doppler measurements, and 3) fused pseudorange and Doppler measurements.

The EKF-tracked position and velocity root-mean-squared errors (RMSEs) were computed for each SV by averaging over the ensemble of 100 MC realizations performed for each SV. These position and velocity RMSEs were then averaged over all 103 SVs tracked in the simulation. Furthermore, open-loop SGP4 propagations of the randomized TLE, which served to initialize the EKFs initial position and velocity estimates, were performed for each MC realization. The average performance of SGP4 is computed in a similar fashion to EKF tracking: an ensemble average over the MC realizations for each SV is then averaged over all SVs. Figs. 4 and 5, respectively, show the position and velocity RMSEs expressed in the RTN frame of the open-loop SGP4-propagated ephemerides as well as the ephemerides tracked using the three different sets of observables: 1) pseudorange measurements, 2) Doppler measurements, and 3) fused pseudorange and Doppler measurements. Fig. 6 shows the magnitude of the
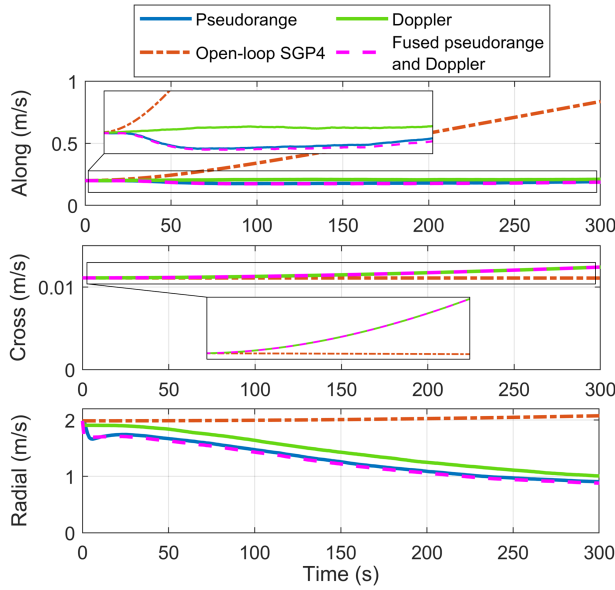
Fig. 5. Velocity RMSEs for tracking using pseudorange, Doppler, and fused pseudorange and Doppler versus SGP4's open-loop position RMSE.
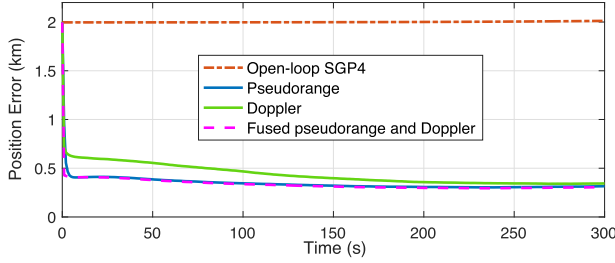

Fig. 6. Magnitude of position error for tracking using pseudorange, Doppler, and fused pseudorange and Doppler versus SGP4's open-loop position error.
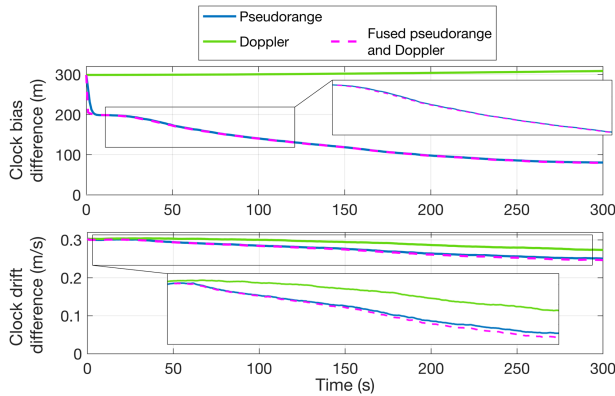

Fig. 7. Clock bias and drift difference RMSEs for tracking using pseudorange, Doppler, and fused pseudorange and Doppler.

LEO SV position error for the open-loop SGP4 propagation and the tracking using the three measurement sets. The EKF-tracked clock states RMSEs were also computed with respect to the simulated clock error states in Section III-C2 by first averaging over the 100 MC realizations for each SV and, then, by averaging over all 103 simulated SVs. Fig. 7

shows the clock error states RMSEs for opportunistic LEO SV tracking with the three different sets of measurements.

This comprehensive MC study reveals the average performance of the opportunistic LEO tracking framework presented in this article. The following conclusions can be made from these simulations. First, it can be seen that the cross-track direction is the least observable for both position and velocity states. This can be explained by the fact that the SVs motion is restricted in the along-track–radial plane. As a result, the cross-track direction is not excited during the SVs motion, which leads to poor estimability of the corresponding states. Second, it can be seen from Figs. 4 to 6 that using pseudorange measurements yield better LEO SV tracking performance than Doppler measurements. Third, fusing both pseudorange and Doppler measurements yields negligible improvements over pseudorange-only tracking. This is suggested by the fact that both types of measurements are highly dependent [cf. (7)], thus leading to a negligible information increase when augmenting the pseudorange measurement vector to include both navigation observables. Fourth, it is worth noting that the clock bias term $c[\delta t_r - \delta t_{\text{leo}}]$ is unobservable with Doppler measurements only and is consequently not actively estimated during LEO SV tracking with this set of observables. This can be seen in the top plot in Fig. 7, where the clock bias RMSE diverges for LEO SV tracking with Doppler measurements. Fifth, the relative clock error states tracking performance is comparable to the relative position and velocity tracking performance with the different sets of measurements: pseudorange observables yield smaller RMSEs than Doppler observables and combining both type of measurements result in a negligible improvement in the tracking performance over pseudorange-only tracking.

IV. EFFECT OF LEO SATELLITE STATE ERRORS ON NAVIGATION PERFORMANCE

This section studies the measurement errors resulting from SVs state errors and analyzes the effect of these measurement errors on the localization error of a stationary unknown receiver.

A. Measurement Errors Due to LEO Satellite State Errors

Let $\hat{\boldsymbol{r}}_{\text{leo}_l}(k)$ and $\hat{\dot{\boldsymbol{r}}}_{\text{leo}_l}(k)$ be the lth LEO SV erroneous position and velocity obtained using TLEs at time-step k, respectively. Define $\tilde{\boldsymbol{r}}_{\text{leo}_l}(k)$ and $\tilde{\dot{\boldsymbol{r}}}_{\text{leo}_l}(k)$ to be the errors at time-step k of propagated LEO ephemerides (e.g., from SGP4) of the lth LEO SV position and velocity, respectively, as

$$\tilde{\boldsymbol{r}}_{\text{leo}_l}(k) \triangleq \boldsymbol{r}_{\text{leo}_l}(k) - \hat{\boldsymbol{r}}_{\text{leo}_l}(k)$$
$$\tilde{\dot{\boldsymbol{r}}}_{\text{leo}_l}(k) \triangleq \dot{\boldsymbol{r}}_{\text{leo}_l}(k) - \hat{\dot{\boldsymbol{r}}}_{\text{leo}_l}(k)$$

where $\boldsymbol{r}_{\text{leo}_l}(k)$ and $\dot{\boldsymbol{r}}_{\text{leo}_l}(k)$ are the lth LEO SV true position and velocity at time-step k, respectively.

Define $c\tilde{\delta t}$ and $c\tilde{\tilde{\delta t}}$ to be the errors in the clock error states estimates as

$$c\tilde{\delta t}_l(k) \triangleq c\left[\delta t_r(k) - \delta t_{\text{leo}_l}(k'_l)\right] - c\left[\hat{\delta t}_r(k) - \hat{\delta t}_{\text{leo}_l}(k'_l)\right]$$

$$c\tilde{\dot{\delta}} t_l(k) \triangleq c\left[\dot{\delta} t_r(k) - \dot{\delta} t_{\mathrm{leo}_l}(k_l')\right] - c\left[\hat{\dot{\delta}} t_r(k) - \hat{\dot{\delta}} t_{\mathrm{leo}_l}(k_l')\right].$$

Next, bounds on pseudorange and pseudorange rate measurement errors are derived as a function of SVs state errors.

1) Bound on Pseudorange Measurements: A receiver only having access to TLEs would produce an estimated pseudorange measurement $\hat{\rho}_l(k)$ to the lth LEO SV as

$$\hat{\rho}_l(k) = \left\|\boldsymbol{r}_r(k) - \hat{\boldsymbol{r}}_{\mathrm{leo}_l}(k_l')\right\|_2 + c\left[\hat{\delta} t_r(k) - \hat{\delta} t_{\mathrm{leo}_l}(k_l')\right] \quad (11)$$

where $c[\hat{\delta} t_r(k) - \hat{\delta} t_{\mathrm{leo}_l}(k_l')]$ is the clock error bias estimate that the receiver's filter maintains. If no prior is available for this clock error bias, different initialization schemes could be implemented, such as initializing this term to zero or setting this term to be the difference between the true measurement and the estimated range, thus effectively setting the value of the clock bias error to make the predicted measurement match the true measurement.

Performing a first-order Taylor series expansion of the erroneous pseudorange measurement estimate $\hat{\rho}_l(k)$ in (11) about the lth LEO SV true position $\boldsymbol{r}_{\mathrm{leo}_l}(k)$ and true clock bias difference $c[\delta t_r(k) - \delta t_{\mathrm{leo}_l}(k_l')]$ yields

$$\hat{\rho}_l(k) \approx \rho_l(k) + \boldsymbol{h}_l^{\mathsf{T}}(k)\tilde{\boldsymbol{r}}_{\mathrm{leo}_l}(k) - c\tilde{\delta} t_l(k) \quad (12)$$

where $\boldsymbol{h}_l(k) \triangleq \frac{\boldsymbol{r}_r(k) - \boldsymbol{r}_{\mathrm{leo}_l}(k_l')}{\|\boldsymbol{r}_r(k) - \boldsymbol{r}_{\mathrm{leo}_l}(k_l')\|_2}$ is the unit line-of-sight (LOS) vector pointing from the lth LEO SV to the receiver at time-step k.

Defining the pseudorange residual $\Delta \rho_l(k)$ of the lth LEO SV as

$$\Delta \rho_l(k) \triangleq \rho_l(k) - \hat{\rho}_l(k)$$

and substituting (12) for $\hat{\rho}_l(k)$ yields

$$\Delta \rho_l(k) \approx -\boldsymbol{h}_l^{\mathsf{T}}(k)\tilde{\boldsymbol{r}}_{\mathrm{leo}_l}(k) + c\tilde{\delta} t_l(k). \quad (13)$$

The magnitude of the range residual $\Delta \rho_l(k)$ can be bounded by invoking the triangular inequality as follows:

$$|\Delta \rho_l(k)| \le \sum_{j=1}^{3} \left|{}^{\{o_l\}} h_l^j(k) {}^{\{o_l\}}\tilde{r}_{\max}^j\right| + c\tilde{\delta} t_{\max} \quad (14)$$

where ${}^{\{o_l\}}\boldsymbol{h}_l(k)$ is $\boldsymbol{h}_l(k)$ expressed in the lth SV RTN frame denoted $\{o_l\}$, ${}^{\{o_l\}}\tilde{\boldsymbol{r}}_{\max}$ is a vector bounding the SVs position errors in the RTN frame (i.e., ${}^{\{o_l\}}\tilde{\boldsymbol{r}}_{\max} \succeq {}^{\{o_l\}}\tilde{\boldsymbol{r}}_{\mathrm{leo}_l}(k)$ for all k, where $\succeq$ denotes the elementwise operation), superscript j indexes the component of vectors ${}^{\{o_l\}}\boldsymbol{h}_l(k)$ and ${}^{\{o_l\}}\tilde{\boldsymbol{r}}_{\max}$, and $c\tilde{\delta} t_{\max} \ge |c\tilde{\delta} t_l(k)|$ for all k.

2) Bound on Pseudorange Rate Measurements: A receiver only having access to TLEs would produce an estimated pseudorange rate measurement $\hat{\dot{\rho}}_l(k)$ to the lth LEO SV as

$$\hat{\dot{\rho}}_l(k) = \left[\dot{\boldsymbol{r}}_r(k) - \hat{\dot{\boldsymbol{r}}}_{\mathrm{leo}_l}(k_l')\right]^{\mathsf{T}} \frac{\left[\boldsymbol{r}_r(k) - \hat{\boldsymbol{r}}_{\mathrm{leo}_l}(k_l')\right]}{\left\|\boldsymbol{r}_r(k) - \hat{\boldsymbol{r}}_{\mathrm{leo}_l}(k_l')\right\|_2} + c\left[\hat{\dot{\delta}} t_r(k) - \hat{\dot{\delta}} t_{\mathrm{leo}_l}(k_l')\right] \quad (15)$$

where $c[\hat{\dot{\delta}} t_r(k) - \hat{\dot{\delta}} t_{\mathrm{leo}_l}(k_l')]$ is the clock error drift estimate that the receiver's filter maintains. If no prior is available for this clock error drift, this term can be initialized to zero.
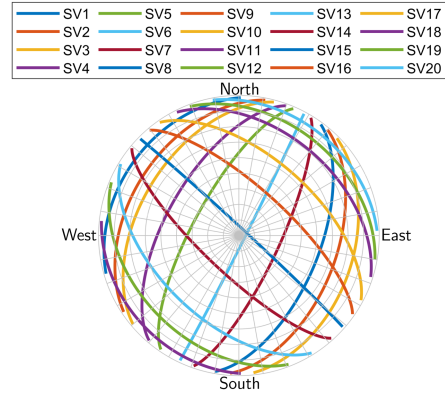

Fig. 8. Skyplot of 20 SVs simulated to validate the bounds.

Performing a first-order Taylor series expansion of the erroneous pseudorange rate measurement estimate $\hat{\dot{\rho}}_l(k)$ in (15) about the lth LEO SV true position $\boldsymbol{r}_{\mathrm{leo}_l}(k)$ and velocity $\dot{\boldsymbol{r}}_{\mathrm{leo}_l}(k)$ and true clock drift difference $c[\dot{\delta} t_r(k) - \dot{\delta} t_{\mathrm{leo}_l}(k_l')]$ yields

$$\hat{\dot{\rho}}_l(k) \approx \dot{\rho}_l(k) + \boldsymbol{g}_l^{\mathsf{T}}(k)\tilde{\boldsymbol{r}}_{\mathrm{leo}_l}(k) + \boldsymbol{h}_l^{\mathsf{T}}(k)\tilde{\dot{\boldsymbol{r}}}_{\mathrm{leo}_l}(k) - c\tilde{\dot{\delta}} t_l(k) \quad (16)$$

where $\boldsymbol{g}_l^{\mathsf{T}}(k) \triangleq \frac{[\dot{\boldsymbol{r}}_r(k) - \dot{\boldsymbol{r}}_{\mathrm{leo}_l}(k_l')]^{\mathsf{T}}}{\|\boldsymbol{r}_r(k) - \boldsymbol{r}_{\mathrm{leo}_l}(k_l')\|_2}\left[\mathbf{I}_{3\times 3} - \boldsymbol{h}_l(k)\boldsymbol{h}_l^{\mathsf{T}}(k)\right]$. Defining the pseudorange rate residual $\Delta \dot{\rho}_l(k)$ of the lth LEO SV as

$$\Delta \dot{\rho}_l(k) \triangleq \dot{\rho}_l(k) - \hat{\dot{\rho}}_l(k)$$

and substituting (16) for $\hat{\dot{\rho}}_l(k)$ yields

$$\Delta \dot{\rho}_l(k) \approx -\boldsymbol{g}_l^{\mathsf{T}}(k)\tilde{\boldsymbol{r}}_{\mathrm{leo}_l}(k) - \boldsymbol{h}_l^{\mathsf{T}}(k)\tilde{\dot{\boldsymbol{r}}}_{\mathrm{leo}_l}(k) + c\tilde{\dot{\delta}} t_l(k). \quad (17)$$

The magnitude of the pseudorange rate residual $\Delta \dot{\rho}_l(k)$ can be bounded by invoking the triangular inequality as follows:

$$|\Delta \dot{\rho}_l(k)| \le \left|{}^{\{o_l\}}\boldsymbol{h}_l^{\mathsf{T}}(k) {}^{\{o_l\}}\tilde{\boldsymbol{r}}_{\max}\right| + \left|\frac{{}^{\{o_l\}}\left[\dot{\boldsymbol{r}}_r(k) - \dot{\boldsymbol{r}}_{\mathrm{leo}_l}(k_l')\right]^{\mathsf{T}}}{\left\|\boldsymbol{r}_r(k) - \boldsymbol{r}_{\mathrm{leo}_l}(k_l')\right\|_2}\right.$$

$$\left.\left[{}^{\{o_l\}}\boldsymbol{h}_l(k) {}^{\{o_l\}}\boldsymbol{h}_l^{\mathsf{T}}(k) - \mathbf{I}_{3\times 3}\right]^{\{o_l\}}\tilde{\boldsymbol{r}}_{\max}\right| + c\tilde{\dot{\delta}} t_{\max} \quad (18)$$

where ${}^{\{o_l\}}\tilde{\boldsymbol{r}}_{\max}$ is a vector bounding the SVs velocity errors in the RTN frame (i.e., ${}^{\{o_l\}}\tilde{\boldsymbol{r}}_{\max} \succeq {}^{\{o_l\}}\tilde{\boldsymbol{r}}_{\mathrm{leo}_l}(k)$ for all k) and $c\tilde{\dot{\delta}} t_{\max} \ge |c\tilde{\dot{\delta}} t_l(k)|$ for all k.

It is important to note that the bounds derived above on pseudorange and pseudorange rate residuals can easily be reduced to bounds on range and range rate measurement residuals by setting the bounds on the clock errors $c\tilde{\delta} t_{\max}$ and $c\tilde{\dot{\delta}} t_{\max}$ to zero in (14) and (18), respectively.

To validate the derived bounds, 20 circular orbits of LEO SVs having an orbital height of 700 km were simulated with various geometries with respect to a receiver stationary on a spherical rotating Earth as can be seen from the skyplot in Fig. 8. SV1 is on the top left quadrant of the skyplot going from West to North and the trajectories of the SVs progressively move until SV10, which goes from South to East in the bottom right quadrant. Similarly, SV11 goes from South to West in the bottom left quadrant of the skyplot and SV20 goes from East to North in the top right
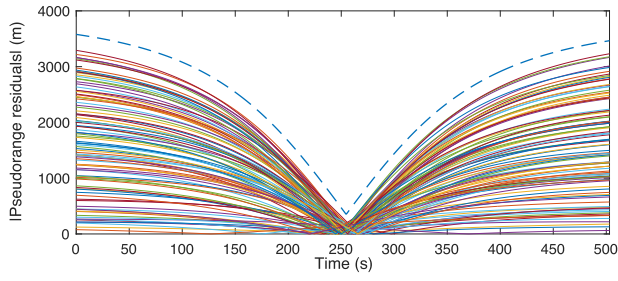
Fig. 9. Magnitude of pseudorange residuals for 100 MC realizations of randomized LEO states (solid) with bound (dashed) for SV 12.
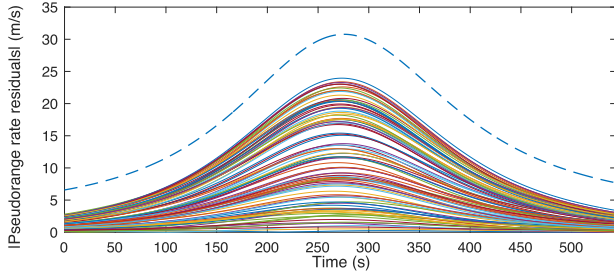

Fig. 10. Magnitude of pseudorange rate residuals for 100 MC realizations of randomized LEO states (solid) with bound (dashed) for SV 2.
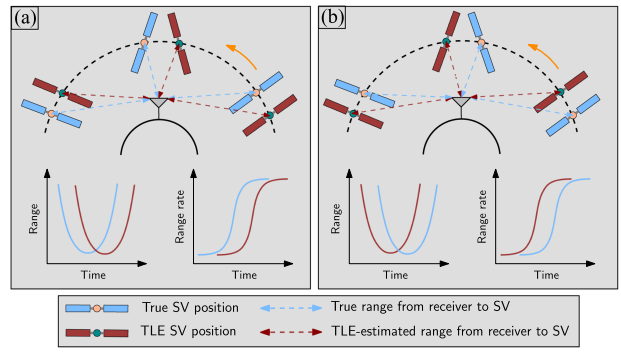

Fig. 11. Schematic to visualize TLE errors' effects on range and range rate residuals. In (a), the TLE-derived SV position lags the true SV position along the orbit while the TLE-derived SV position leads the true SV position along the orbit in (b).

quadrant. Each of these 20 orbits was randomized in 100 MC runs with position errors drawn from a uniform distribution with maximum magnitude ${}^{\{b\}}\tilde{r}_{max} \triangleq [4 \times 10^3, 20, 200]^{\mathsf{T}}$ m in the LEO SVs RTN frame to emulate TLE errors. The velocities were then modified accordingly to maintain the circularity of the orbit and ${}^{\{b\}}\tilde{\dot{r}}_{max}$ was taken to be the maximum velocity errors in the LEO SVs RTN frame's axes. Furthermore, clock bias and drift errors were introduced for the receiver's and LEO SVs oscillators. It is first assumed, without loss of generality, that the oscillator of the receiver and the LEO SV are nominally synchronized (i.e., the true pseudorange and pseudorange rate measurements are in fact range and range rate measurements, respectively). Then, the maximum deviation from the nominally synchronized clock states is set to 100 and 10 ns for the receiver's and LEO SVs clock biases, respectively, and to 1 and 0.1 ns/s for the receiver's and LEO SVs clock drifts, respectively, when generating the simulated pseudorange and pseudorange rate measurements according to (6) and (8), respectively. Consequently, $c\tilde{\delta t}_{max}$ and $c\tilde{\dot{\delta t}}_{max}$ are taken to be equal to $c[(100 + 10) + (1 + 0.1)t_{vis}] + 10^{-9}$ m and $c(1 + 0.1) \times 10^{-9}$ m/s, respectively, where t_{vis} is the duration (in seconds) of the LEO SV visibility from the receiver.

The magnitude of pseudorange and pseudorange rate residuals for the 100 MC realizations as well as the derived bounds in (14) and (18) for 2 SVs are shown in Figs. 9 and 10, respectively. It can be seen that the derived bounds are valid for the entire duration of LEO SV visibility and for all MC realizations. Moreover, similar behavior was observed for all the 20 simulated SVs.

Finally, it is worth noting that pseudorange measurement residuals change signs at around the time the SV passes the zenith in its trajectory with respect to the receiver while pseudorange rate measurement residuals do not change signs (i.e., either remain positive or negative for the entire duration of the SV pass). This can be explained by the fact that most of the TLE position errors are in the along-track direction of the SVs motion as has been observed experimentally (this will be discussed in Section V, cf. Fig. 19), which leads to the TLE-derived SV position to either lag or lead the true SV position along the orbit as depicted in Fig. 11(a) and (b), respectively. In the case where the TLE-derived SV position lags the true SV position, the TLE-derived range between the receiver and the SV is initially greater than the true range between the receiver and the SV, then both ranges become equal at around the SVs zenith, and finally, the true range becomes greater than the TLE-derived range, thus resulting in residuals continuously going from negative to positive values along the pass. The opposite happens when the TLE-derived position leads the true SV position: range residuals are initially positive, then cross zero at around the zenith, before becoming negative. TLE errors in the cross-track and radial directions, and more importantly clock bias errors, result in the pseudorange residuals not crossing zero at exactly the SVs zenith. For range rate measurements, both the true range and the TLE-derived range decrease (negative range rate) before reaching the closest point to the receiver (zero range rate) and then increase afterward (positive range rate) but the lag/lead of the TLE-derived SV position results in a shifted range rate curve with respect to the true range rate curve. These two curves do not overlap, meaning there will be no sign shift in the range rate residuals, and the separation between them is the greatest at around the SVs zenith which explains the higher magnitudes of pseudorange rate residuals around the SVs zenith in Fig. 10. Furthermore, the time evolution of the true and TLE-derived ranges and range rates are depicted in Fig. 11 for both the case when the TLE-derived SV position lags (a) and leads (b) the true SV position to facilitate

the visualization of these claims on range and range rate residuals sign change.

B. State Estimation Errors Due to Measurement Errors

To study the propagation of errors from the measurements to the estimated receiver's states x (consisting of the stationary 3-D ECEF position r_r and clock error states x_{clk}), assume first that the receiver's states are perfectly known (e.g., through optimal filtering of measurements with knowledge of the ground truth LEO SV ephemeris). Then, errors in the LEO SVs ephemeris and clock error states are suddenly introduced in the receiver's knowledge. This will consequently lead to discrepancies between the extracted measurements, which are consistent with the true SVs ephemeris and nominal clock error states, and the predicted measurements by the receiver using the erroneous ephemeris and clock error states information. These discrepancies will cause the receiver to update the estimates of its states to fit the measurements extracted from the LEO SVs signals to its erroneous model. This perturbation analysis can be captured in one iteration of the nonlinear least-squares (NLS) as

$$\Delta x = \left(H^{\mathsf{T}} H \right)^{-1} H^{\mathsf{T}} \Delta z \qquad (19)$$

where Δx is the state estimate error vector, H is the measurement Jacobian matrix, and $\Delta z = [\Delta z(1), \ldots, \Delta z(K)]^{\mathsf{T}}$ is the measurement innovations vector for the entire duration of satellite visibility, with K being the last time-step index. The stationary receiver's clock error states consist of the differenced clock error bias and drift between the receiver's and the SVs oscillator when using pseudorange measurements but only the differenced drift error states when using pseudorange rate measurements.

Although several iterations are usually required for the NLS estimator to converge, one iteration captures the majority of the errors introduced in the receiver state estimates, since the perturbation in the LEO SVs states is relatively small (i.e., TLE ephemeris errors are negligible compared to the distance between the receiver and LEO SV and do not considerably affect the unit LOS vector between the receiver and LEO SV).

One way to bound the receiver state estimation error Δx is by invoking the Cauchy–Schwarz inequality on (19) as follows:

$$\|\Delta x\|_2 \leq \left\| \left(H^{\mathsf{T}} H \right)^{-1} H^{\mathsf{T}} \right\|_2 \|\Delta z\|_2 \qquad (20)$$

where $\|A\|_2 = \sigma_{max}(A)$, i.e., the maximum singular value of the matrix A.

In Section IV-A, a bound on $|\Delta z(k)|$ was found for all k as a function of the receiver-SV geometry; maximum LEO SV ephemeris errors ${}^{\{b\}}\tilde{r}_{max}$ and ${}^{\{b\}}\tilde{\dot{r}}_{max}$, expressed in the SVs RTN frame, and maximum clock bias $c\tilde{\delta}t_{max}$ and drift $c\tilde{\dot{\delta}}t_{max}$ errors, for $z \in \{\rho, \dot{\rho}\}$.

Since the pseudorange rate residuals do not change sign (i.e., either remain positive or negative) during the LEO SV visibility period as explained in Section IV-A and as can be seen from Fig. 10, $\|\Delta \dot{\rho}\|_2$ can easily be bounded by $\|\Delta \dot{\rho}'\|_2$
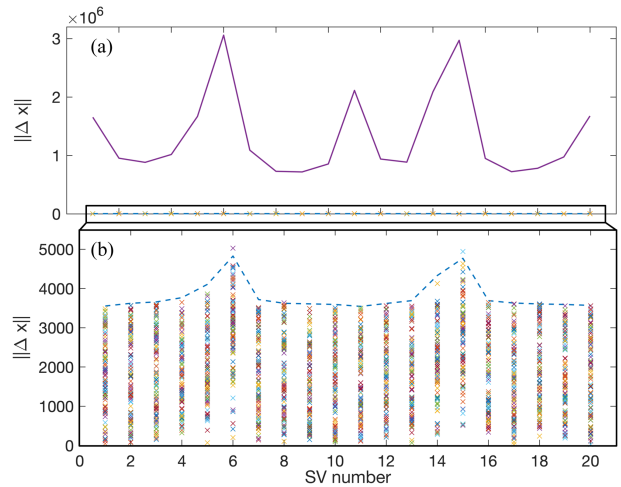

Fig. 12. Magnitude of receiver state estimation error for 100 MC realizations of randomized ephemerides (cross) with bound (solid) and tight bound approximation (dashed) computed using pseudorange measurements for each of the 20 SVs shown in Fig. 8.

where each component of $\Delta \dot{\rho}'$ is computed from (18). Using (20), this yields the following upper bound on receiver state estimation errors:

$$\left\| \Delta x_{\dot{\rho}} \right\|_2 \leq \left\| \left(H_{\dot{\rho}}^{\mathsf{T}} H_{\dot{\rho}} \right)^{-1} H_{\dot{\rho}}^{\mathsf{T}} \right\|_2 \left\| \Delta \dot{\rho}' \right\|_2 \qquad (21)$$

which is represented by the solid line in Fig. 13.

Pseudorange residuals, however, switch sign around the LEO SVs zenith (i.e., maximum elevation angle) with respect to the receiver as demonstrated in Section IV-A and as can be seen in Fig. 9.

As a result of this sign change in $\Delta \rho$, (14) has to be modified resulting in $\Delta \rho'(k) \triangleq {}^{\{b\}} h^{\mathsf{T}}(k) {}^{\{b\}} \tilde{r}_{max} + c \tilde{\delta} t_{max}$. Unfortunately, although $\|\Delta \rho'\|_2$ is greater than $\|\Delta \rho\|_2$ for the majority of realizations, this is not guaranteed. As a result, the strict bound in (21) is not transposable to pseudorange measurements. In practice, however, using the equivalent of (21) with pseudorange measurements yields a very loose upper bound on the magnitude of the state estimation errors, which is 3 orders of magnitude greater than the actual errors and is, thus, too loose to be useful, as seen in Fig. 12. This can be explained by the fact that only a small component of the vectors $\Delta \rho'$ and $\Delta \dot{\rho}'$ are scaled by the maximum singular value of the linear map $(H^{\mathsf{T}} H)^{-1} H^{\mathsf{T}}$, where H is the corresponding measurement Jacobian for each observable type. Effectively, $\Delta \rho'$ and $\Delta \dot{\rho}'$ are almost orthogonal to the right singular vector associated with the maximum singular value of $(H^{\mathsf{T}} H)^{-1} H^{\mathsf{T}}$ with respective angles of $90.04°$ and $90.06°$ on average for all SVs of Fig. 8. Additionally, the looseness of the bound for pseudorange compared to pseudorange rate stems from the fact that $\|\Delta \rho'\|_2 \gg \|\Delta \dot{\rho}'\|_2$.

Another way to approximate the magnitude of receiver state estimate errors resulting from errors in measurements is by plugging in $\Delta z'$ in (19) resulting in

$$\|\Delta x_z\|_2 \approx \|\Delta x_z'\|_2 = \left\| \left(H_z^{\mathsf{T}} H_z \right)^{-1} H_z^{\mathsf{T}} \Delta z' \right\|_2, \ z \in \{\rho, \dot{\rho}\}. \qquad (22)$$
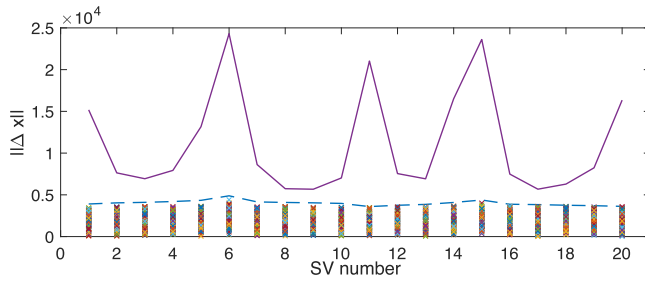
Fig. 13. Magnitude of receiver state estimation error for 100 MC realizations of randomized ephemerides (cross) with bound (solid) and tight bound approximation (dashed) computed using pseudorange rate measurements for each of the 20 SVs shown in Fig. 8.

The previous expression is not a strict bound *per se* as it is slightly violated for only 3 realizations (out of 2000 for pseudorange measurements with less than 4.2% error) but rather a good approximation of the maximum magnitude of receiver state estimate errors as depicted in Figs. 12(b) and 13. Note that the realizations for which the approximation in (22) does not overbound the magnitude of the state estimation errors occur mainly for SVs with high maximum elevation angles with respect to the receiver (i.e., SV6 and SV15 as can be seen from the skyplot in Fig. 8). It is also interesting to observe that these SVs with high maximum elevation angles approach the singular unobservable case in which the receiver is in the orbital plane (i.e., maximum elevation angle of $90°$ with nonrotating Earth) [67] and that this reduction in estimability is reflected in the higher value of both the magnitude of state estimation errors (crosses) and the tight approximation of the upper bound (dashed) in Fig. 12(b) for these SVs. The intuition for this approximation results from the fact that (19) is the vector, which premultiplied by $\mathbf{H}$ gives the orthogonal projection of $\Delta\mathbf{z}$ onto the range space of $\mathbf{H}$, thus resulting in the least squares solution. Similarly, $\mathbf{H}\Delta\mathbf{x}'$ gives the orthogonal projection of $\Delta\mathbf{z}'$ onto the range space of $\mathbf{H}$ in (22). Assuming $|\Delta\mathbf{z}'| \succeq |\Delta\mathbf{z}|$ (which is always true for $\mathbf{z} = \dot{\rho}$ but not guaranteed for $\mathbf{z} = \rho$), a sufficient condition to ensure that $\|\Delta\mathbf{x}'\|_2 \geq \|\Delta\mathbf{x}\|_2$ is to have $\mathbf{v}_i \succeq \mathbf{0}$ or $\mathbf{v}_i \preceq \mathbf{0}$, where $\mathbf{v}_i$ are the vectors forming the orthonormal basis of the range space of $\mathbf{H}$ with $i = 1, \ldots, n$ where n is the number of estimated states. This condition ensures that the coordinates of the projection of $\Delta\mathbf{z}'$ onto the range space of $\mathbf{H}$ expressed in the orthornormal basis are elementwise greater in absolute value than their counterparts for the projection of $\Delta\mathbf{z}$, which, in turn, implies $\|\Delta\mathbf{x}'\|_2 \geq \|\Delta\mathbf{x}\|_2$. It is interesting to note that the vectors forming the orthonormal basis of the range space of $\mathbf{H}$ for pseudorange measurements of SV6 and SV15 have entries that often fluctuate signs. This behavior is suspected to cause the upper bound approximation in (22) to underestimate the magnitude of state estimation errors for some realizations for these high maximum elevation angle SVs.

Finally, as in the opportunistic LEO SV tracking with Doppler measurements in Section III, note that the difference between the receiver's and LEO SVs clock bias is not estimated in localization since this quantity is not observable with pseudorange rate measurements. As a result, the receiver state estimation error vector $\Delta\mathbf{x}_{\dot{\rho}}$ is composed of only 4 elements, whereas $\Delta\mathbf{x}_{\rho}$ has 5 entries. It is also interesting to note that the estimation errors in the clock error states are negligible with respect to the error in the receiver's estimated 3-D position. Consequently, the magnitude of position error and both tight upper bound approximation and strict loose upper bound on position errors are indistinguishably below the magnitude of all state errors represented, respectively, by the crosses, dashed line, and solid line in Figs. 12 and 13.

V. EXPERIMENTAL RESULTS

This section presents the results of an experiment performed with a stationary receiver on the University of California, Irvine, USA campus opportunistically extracting carrier phase navigation observables from an Orbcomm LEO SV's downlink signals. The Orbcomm LEO constellation was chosen for this experiment as Orbcomm SV's openly transmit ephemeris information obtained from their onboard GPS receivers in their downlink signals [68]. As a result, the receiver can decode this accurate ephemeris information, which will serve as a ground truth to assess the performance of the LEO SV tracking framework developed in this article in comparison to the open-loop SPG4-propagated TLE ephemeris. Additionally, the ground truth ephemeris will also serve to verify the bounds derived in Section IV.

A. Experimental Setup and Filter Settings

A very-high frequency antenna was connected to an Ettus E312 Universal Software Radio Peripheral (USRP) to receive Orbcomm downlink signals at 137–138 MHz and sample them at 2.4 MS/s. The USRPs oscillator was driven by an external, freely-running CDA-2990 OctoClock. The receiver was placed on the top of a parking structure in an open sky environment to prevent multipath effects. Carrier phase navigation observables were opportunistically extracted by the receiver and were corrected for ionospheric and tropospheric effects using standard models from the work in [66]. These measurements were then filtered at a rate of 1 Hz in the EKF developed in Section III-A to perform the tracking of the Orbcomm FM107 SV for around 6 min.

The LEO SV's position and velocity estimates were initialized from the SGP4-propagated ephemeris of the most recent TLE available for the Orbcomm FM107 SV tracked in this experiment. The associated initial position and velocity covariances were set to $^o\mathbf{P}_{\mathbf{x}_r}(0|0) \triangleq \mathrm{diag}[10^7, 10^3, 10^4]$ m^2 and $^o\mathbf{P}_{\dot{\mathbf{x}}_r}(0|0) \triangleq \mathrm{diag}[10^{-2}, 10^{-1}, 10^2]\,(\mathrm{m/s})^2$ in the SV's RTN frame, respectively. The Orbcomm FM107 SV's initial position and velocity covariance were set to be consistent

TABLE II
Experimental Oscillator Parameters

Quality	Coefficients $\{h_0, h_{-2}\}$
Typical-quality TCXO	$\{9.4 \times 10^{-20}, 3.8 \times 10^{-21}\}$
High-quality OCXO	$\{2.6 \times 10^{-22}, 4.0 \times 10^{-26}\}$

with the observed SGP4-propagated TLE ephemeris errors (computed with respect to the truth ephemeris that is obtained by decoding it from the Orbcomm SV's downlink signals). It is worth noting that such magnitude of errors (with more than 7-km along-track error as shown in Fig. 19) is not common for TLEs and may have been caused by the Orbcomm SV performing a maneuver that altered the ballistic trajectory that was fit in the TLE published by NORAD. The covariance about the SV's orbital states in the simulations of Section III-D was selected to be more representative of the actual errors expected from a TLE. It is stated in [69] that the position error of TLEs is usually around 1 km at epoch and grows with the propagation time. The daily cadence of TLE updates for SV's in LEO results in the ephemeris errors being usually on the order of a 1–3 km at any point in time. In practical situations where initial covariance sizing cannot be performed to be consistent with the TLE errors since the SV's truth ephemeris is not known, a bank of filters with different initial covariance sizes can be implemented in a multiple-model estimation framework. The better-matched filter with the most appropriate covariance size will have the most consistent innovation residuals than the other more mismatched filters. Consequently, the best-matched filter's state estimate and associated covariance will dominate the other filters' in the combination step of the multiple-model estimator and the unknown initial covariance sizing problem is circumvented.

Since carrier phase measurements are used in this experiment, the clock bias difference term of $\boldsymbol{x}_{\mathrm{clk}}$ is modified by adding the carrier phase ambiguity term from (9) and becomes $c[\delta t_r - \delta t_{\mathrm{leo}}] + \lambda N$. This term is initialized by subtracting the initial estimated range from the first carrier phase measurement. The clock drift term was initialized to 0 and the clock error states' covariance was initialized to $\mathbf{P}_{\boldsymbol{x}_{\mathrm{clk}}} \triangleq \mathrm{diag}[10^7, 10^2]$ with units of $[\mathrm{m}^2, (\mathrm{m/s})^2]$ corresponding to a 1σ of around 11 μs and 33 ns/s for the clock bias and drift, respectively.

The process noise covariance of the Orbcomm SV's orbital motion was set to ${}^o\bar{\mathbf{Q}}_{\boldsymbol{r}\dot{\boldsymbol{r}},\mathrm{emp}}$ found in Section III-B, where ${}^o\bar{\mathbf{Q}}_{\boldsymbol{r}\dot{\boldsymbol{r}},\mathrm{emp}}$ was rotated to the ECI frame at each time-step to propagate the estimation error covariance of the LEO SV's position and velocity states. The process noise covariance of the clock error states was set to be equivalent to a combination of a typical-quality temperature-compensated crystal oscillator (TCXO)–high-quality OCXO pair. The power-law coefficients of these oscillators are given in Table II. This choice was motivated by findings in [44] that characterized the combined oscillators' quality for the clock onboard Orbcomm SVs and the CDA-2990 OctoClock used to discipline the receiver's clock in this experiment. The time-varying measurement noise variance was set to be
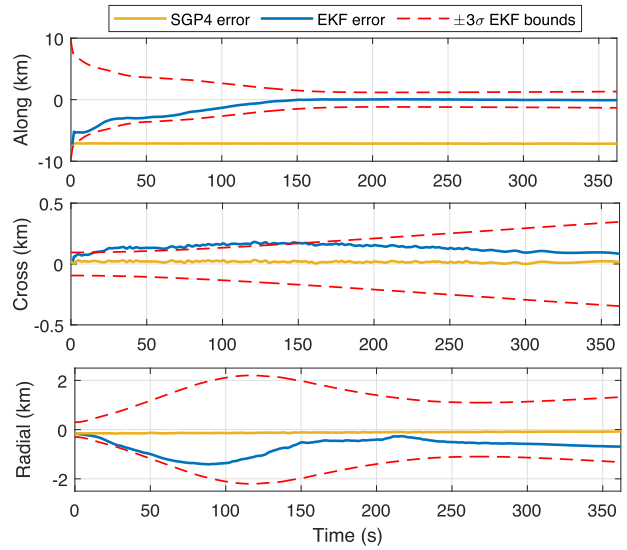

Fig. 14. EKF-tracked position errors with associated $\pm 3\sigma$ bounds versus open-loop SGP4 errors for Orbcomm FM107 SV.
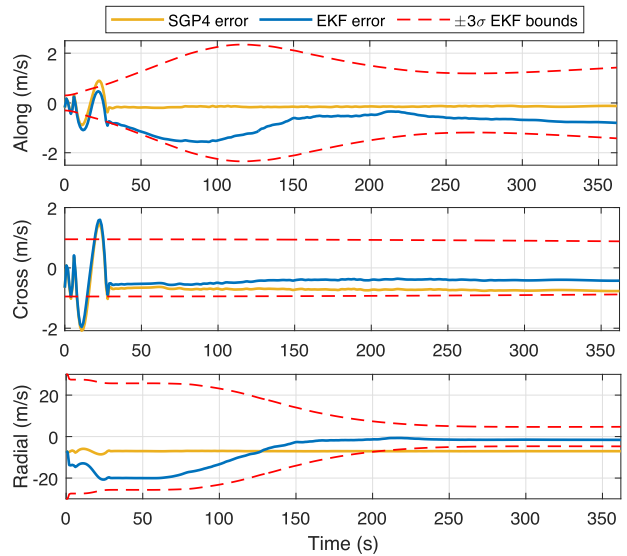

Fig. 15. EKF-tracked velocity errors with associated $\pm 3\sigma$ bounds versus open-loop SGP4 errors for Orbcomm FM107 SV.

proportional to the inverse of the predicted C/N_0 from (10), expressed in linear units, and it ranged between 3.49 and 4.84 m^2.

B. Experimental Tracking Results

Figs. 14 and 15, respectively, show the position and velocity EKF error plots and associated $\pm 3\sigma$ bounds as well as the open-loop SGP4-propagated ephemeris errors in the SV's RTN frame. Figs. 16 and 17, respectively, show the 3-D position and velocity errors magnitude for the EKF-tracked and the open-loop SGP4-propagated ephemeris. The initial position and velocity errors of over 7.1 km and 7.3 m/s obtained from the SGP4 propagation of the most recent TLE of the Orbcomm FM107 SV were reduced to final errors of 698.7 m and 1.8 m/s, respectively, in just over 6 min. of tracking.
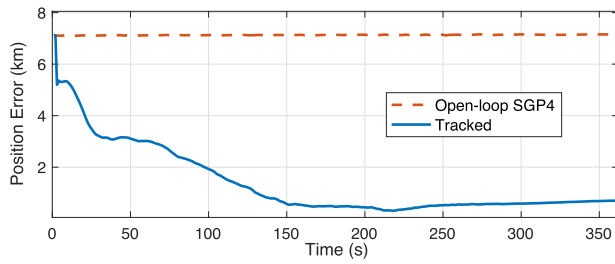
Fig. 16.   EKF-tracked 3-D position error magnitude versus open-loop SGP4 errors for Orbcomm FM107 SV.
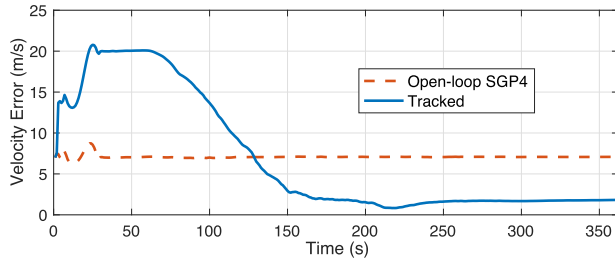

Fig. 17.   EKF-tracked 3-D velocity error magnitude versus open-loop SGP4 errors for Orbcomm FM107 SV.

The following are key takeaways from these experimental tracking results. First, note that the LEO SV tracking performance with carrier phase observables is similar to that using pseudorange measurements as both measurement models only differ by the carrier phase ambiguity (6)–(9) and the effect of the ionosphere on the measurements: δt_{iono} acts as delay for pseudoranges and as an advance for carrier phases. After correcting for the atmospheric effects, accounting for the carrier phase ambiguity term is done by lumping it with the clock bias difference term estimated in the filter. Second, as can be seen from Figs. 14 and 15, the open-loop SGP4-propagated ephemeris errors stay relatively constant over the entire experiment. Moreover, opportunistic tracking mostly reduces the along-track position and radial velocity errors, which are usually where most of the errors in ephemerides obtained from TLEs lie. The radial position and along-track velocity errors, however, increase slightly during tracking as compared to their open-loop SGP4 counterparts. Third, as demonstrated in simulations in Section III-E, the cross-track direction is verified experimentally to be the least observable for both position and velocity. Fourth, note that the oscillations observed in the Orbcomm SV's velocity EKF plots in Fig. 15 between 0 and 30 s are due to the noisy decoding of the ground truth ephemeris information transmitted by the SV in its downlink signals. This happens at the beginning of the tracking period as the Orbcomm SV's elevation is still low (below $16°$ before 30 s), thus leading to errors in the ephemeris packet decoding as a result of low C/N_0.

C.   Experimental Receiver Localization Results

To demonstrate the practical advantages of LEO SV ephemeris refinement via the opportunistic tracking framework presented in this article, an EKF is implemented to localize another stationary receiver extracting measurements opportunistically from Orbcomm FM107 SV's downlink signals using the open-loop SGP4-propagated ephemeris on one hand and the refined ephemeris resulting from the tracking performed in Section V-B by the tracking receiver on the other hand. It is assumed that the receiver to be localized has knowledge of its height (e.g., through altimeter measurements). Since the localization of the unknown receiver serves the purpose of demonstrating the efficacy of the tracking receiver in refining the satellite's ephemeris over the publicly available knowledge in TLE files, the unknown receiver was placed in an open sky environment. As such, multipath effects are also ignored in this case for the simplicity of this proof of concept.

The state vector estimated by the EKF is $x \triangleq [r_r^{\mathrm{T}}, x_{\mathrm{clk}}^{\mathrm{T}}]$, where r_r is the receiver' 3-D position in the ECEF reference frame and x_{clk} is the same as in Section V-B with the carrier phase ambiguity term added to the clock bias difference. Since the fixed ECEF position of the receiver is estimated, the Orbcomm SV's ephemeris is also computed in the ECEF frame, denoted $\{e\}$. The TLE-generated ephemeris $^e x_{\mathrm{leo,SGP4}}$ is computed by performing the SGP4 propagations of the most recent TLE for the Orbcomm FM107 SV in the ECEF frame. The refined ephemeris is obtained by propagating backward in time the last tracked position and velocity estimate in the ECI frame by numerical integration of the two-body with J_2 equations of motion (3). This is done since the last state estimate produced by the tracking receiver is the most refined state vector describing the SV's ephemeris. Consequently, the backward propagation from this most refined state vector results in the most refined orbit for the SV's ECI ephemeris, which is then rotated to ECEF to yield the refined ephemeris $^e x_{\mathrm{leo,tracked}}$ that is used by the stationary receiver localizing itself. It is worth mentioning that this tracked ephemeris back propagation is performed in post-processing in these experimental results, i.e., the last SV position and velocity states estimated by the tracking receiver at the end of the SV's pass are used in the refined ephemeris computation. However, this is not required as one can have such a system operating in real-time: the most up-to-date estimated state vector by the tracking receiver can be propagated via the SV's dynamics to generate the refined ephemeris that is fed to the receiver localizing itself. This process can run sequentially as the tracking receiver continues refining the ephemeris of the LEO SV over the duration of its pass while the unknown receiver keeps on improving its localization performance with the incrementally improved ephemeris it gets from the tracking receiver.

The EKF using the SGP4 open-loop ephemeris $^e x_{\mathrm{leo,SGP4}}$ and the EKF using the refined ephemeris $^e x_{\mathrm{leo,tracked}}$ were both initialized with the same initial receiver position estimate, drawn from a Gaussian distribution with the mean being the true receiver's location and a variance of $10^8 \ \mathrm{m}^2$ in the East and North directions as seen in Fig. 18. The initial receiver position error was 13.48 km. The clock error states' covariance was initialized to $\mathbf{P}_{x_{\mathrm{clk}}} \triangleq \mathrm{diag}[10^8, 10^2]$ with units of $[\mathrm{m}^2, (\mathrm{m/s})^2]$ corresponding to a 1σ of around 33 μs
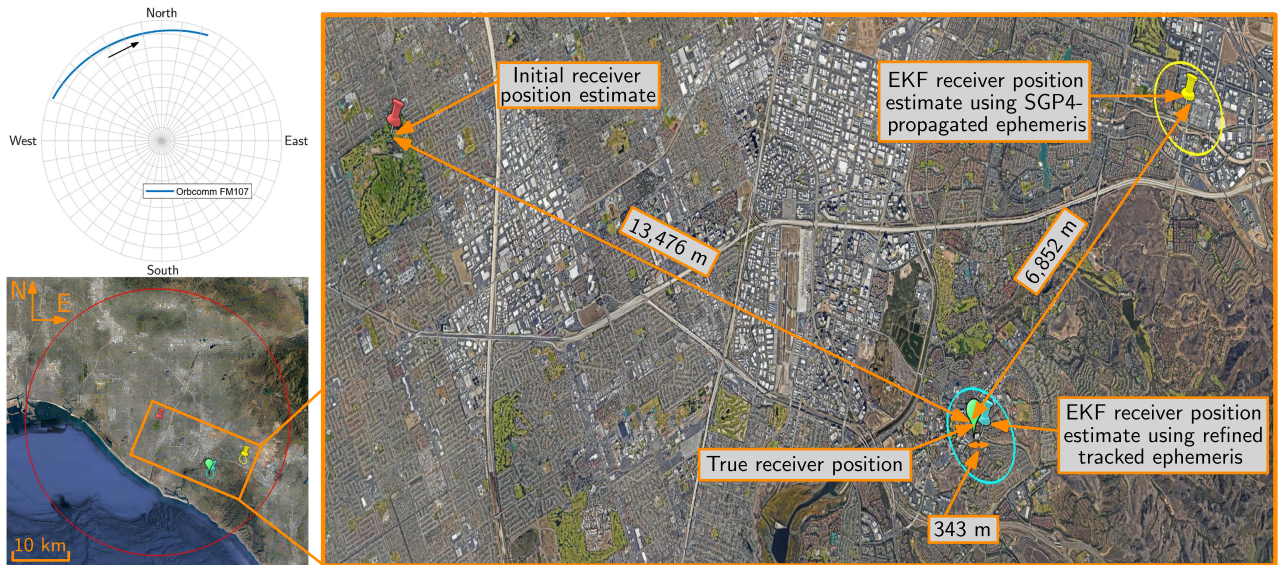
Fig. 18. Experimental results: skyplot of Orbrcomm LEO SV trajectory and true receiver position (green) along with estimates and corresponding 95th-percentile horizontal uncertainty ellipses: 1) red: Initial estimate, 2) yellow: EKF using $^e\boldsymbol{x}_{\text{leo,SGP4}}$ ephemeris, and 3) blue: EKF using $^e\boldsymbol{x}_{\text{leo,tracked}}$ ephemeris. Map data: Google Earth.

TABLE III
Horizontal 2-D Positioning Errors for EKF Using Open-Loop
SGP4-Propagated Ephemeris and EKF Using Refined
Tracked Ephemeris

	Initial	Final (SGP4)	Final (refined)
Horizontal error (m)	13,476	6,852	343

and 33 ns/s for the clock bias and drift, respectively. The clock error states process noise covariance and time-varying measurement noise were identical to those in Section V-B.

The experimental localization results are shown in Fig. 18 and Table III and are summarized next. The 2-D positioning error of the receiver localized using the refined tracked ephemeris $^e\boldsymbol{x}_{\text{leo,tracked}}$ was decreased from its initial value of around 13.48 km to 343 m while the localization performed using the SGP4-propagated ephemeris $^e\boldsymbol{x}_{\text{leo,SGP4}}$ diverged to over 6.85 km in error. The localization estimate using the $^e\boldsymbol{x}_{\text{leo,SGP4}}$ is inconsistent as its associated uncertainty ellipse does not include the true receiver position (green pin is outside the yellow ellipse in Fig. 18). This is due to a model mismatch, as the SGP4-propagated ephemeris fed to the EKF is over 7.13 km away from the true SV's ephemeris, on average, and is causing filter divergence [70]. Additionally, note that the shape, size, and orientation of the uncertainty ellipses of both EKFs in Fig. 18 are similar. This is explained by both EKFs having the same initial estimation error covariance, process noise covariance, time-varying measurement noise, and the fact that the measurement Jacobians of both EKFs are nearly identical: the time history of the unit LOS vectors pointing from the SV to the estimated receiver location are very close for both $^e\boldsymbol{x}_{\text{leo,tracked}}$ and $^e\boldsymbol{x}_{\text{leo,SGP4}}$.
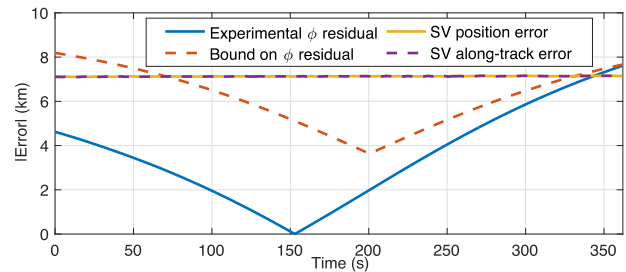

Fig. 19. Experimental carrier phase residuals magnitudes along with bound and 3-D position error with its along-track component for Orbcomm FM107 SV.
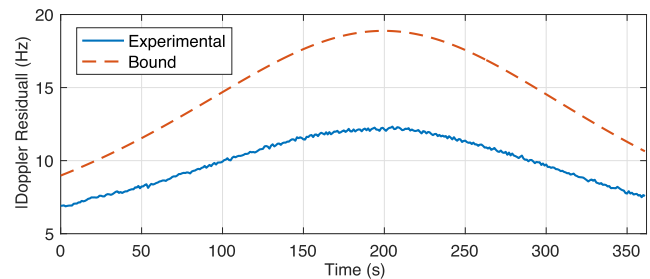

Fig. 20. Experimental Doppler residuals magnitudes along with bound for Orbcomm FM107 SV.

D. Experimental Bound Validation

In this section, the derived results of Section IV are verified with the data from the Orbcomm FM107 SV experiment. Figs. 19 and 20 show the magnitudes of the carrier phase and Doppler residuals along with the corresponding bounds from (14) and (18) scaled by f_c/c, respectively. The residuals were calculated by subtracting the predicted measurements computed from (9) and (7)–(8)

	TLE ephemeris	Bound approximation	Loose bound
$\left\| \boldsymbol{\Delta x_\phi} \right\|_2 (\times 10^3)$	6.8	7.1	1.0×10^4
$\left\| \boldsymbol{\Delta x_{f_D}} \right\|_2 (\times 10^3)$	3.7	6.8	2.8×10^3

Values are in meters.

using the TLE-generated ephemeris from the true measurements extracted by the receiver. The differenced clock bias and drift states used in the predicted measurement calculations were set to the difference between the first carrier phase measurement and the initial true range, and zero, respectively, to focus on the effects of the TLE errors on the measurement residuals. The maximum LEO SV's state errors ${}^{\{b\}}\tilde{\boldsymbol{r}}_{\max}$, ${}^{\{b\}}\tilde{\dot{\boldsymbol{r}}}_{\max}$, $c\tilde{\delta}t_{\max}$, and $c\dot{\tilde{\delta}}t_{\max}$ were computed using the TLE-propagated ephemeris, the ground truth decoded ephemeris, and the true measurements. Fig. 19 also shows the 3-D position error of the Orbcomm FM107 SV's TLE-derived ephemeris along with its component in the SV's RTN frame, demonstrating that most of the TLE-propagated ephemeris position error is the along-track direction. It is interesting to note that the experimental carrier phase residual switches signs around 50 s earlier than the minimum of the bound curve that corresponds to an approximation of the SV's zenith in Fig. 19. This 50-s difference is caused by the discrepancy in the clock bias term between the true and predicted measurements, which results in the true and predicted carrier phase curves having the same value when the SV is not yet at zenith, i.e., residual curve crossing zero before zenith. Table IV shows the magnitude of the receiver's states estimation errors from one iteration of the NLS (19) using carrier phase and Doppler measurements. The approximation of a tight upper bound and the strict loose upper bound on this magnitude are also computed. Note that the results in Table IV are consistent with those observed in simulations in Figs. 12 and 13.

VI. CONCLUSION

This article presented a complete framework to perform LEO SVs tracking by a receiver opportunistically extracting navigation observables from their downlink signals. The performance of the tracking filter was studied via MC simulations for 103 SVs with diverse geometries with respect to the receiver and for three different sets of observables: 1) pseudorange, 2) Doppler, and 3) fused pseudorange and Doppler measurements. Additionally, the performance of the tracking filter was compared to the average performance of the open-loop SGP4 propagation of randomized TLE realizations. This comparison revealed the ephemeris refinement capability of the tracking filter, particularly in the along-track position and radial velocity, where most of the TLE-propagated ephemeris errors lie. Additionally, bounds on pseudorange and Doppler residuals were derived and the magnitude of stationary receiver state estimation errors were characterized as a function of LEO

SVs state errors. In other words, the error propagation from the LEO SVs state space to the measurement space to the receiver's state space was analyzed. Finally, experimental results were presented demonstrating the performance of the opportunistic tracking framework and error propagation analysis. The initial position error of the Orbcomm FM107 SV calculated from TLE-derived ephemeris was reduced by an order of magnitude. Receiver localization via an EKF with the tracked ephemeris from the Orbcomm FM107 LEO SV showed the initial horizontal error reducing from 13,476 m to 343 m. In contrast, it was shown that if the EKF employed SGP4 propagated ephemeris, the error reduced to 6,852, but dangerously, the filter's estimate was inconsistent. Finally, the observed experimental errors are contained within the derived bounds.

REFERENCES

[1] Union of Concerned Scientists, "UCS satellite database," Jan. 2022. [Online]. Available: https://www.ucsusa.org/resources/satellite-database

[2] L. Boldt-Christmas, "Low Earth orbit," Mar. 2020. [Online]. Available: http://www.esa.int/ESA_Multimedia/Images/2020/03/Low_Earth_orbit

[3] D. Bhattacherjee et al., "Gearing up for the 21st century space race," in *Proc. ACM Workshop Hot Topics Netw.*, 2018, pp. 113–119.

[4] S. Clark, "SpaceX passes 2,500 satellites launched for Starlink internet network," May 2022. [Online]. Available: https://spaceflightnow.com/2022/05/13/spacex-passes-2500-satellites-launched-for-companys-starlink-network/

[5] J. Brodkin, "SpaceX says 12,000 satellites isn't enough, so it might launch another 30,000," Oct. 2019. [Online]. Available: https://arstechnica.com/information-technology/2019/10/spacex-might-launch-another-30000-broadband-satellites-for-42000-total

[6] A. Boley and M. Byers, "Satellite mega-constellations create risks in Low Earth Orbit, the atmosphere and on Earth," *Sci. Rep.*, vol. 11, no. 1, pp. 1–8, 2021.

[7] D. Kessler, N. Johnson, J.-C. Liou, and M. Matney, "The Kessler syndrome: Implications to future space operations," *Adv. Astronautical Sci.*, vol. 137, no. 8, pp. 1–15, 2010.

[8] J. Nicholas, "The collision of Iridium 33 and Cosmos 2251: The shape of things to come," in *Proc. Int. Astronautical Congr.*, 2009, pp. 1–14.

[9] J.-C. Liou and N. Johnson, "Instability of the present LEO satellite populations," *Adv. Space Res.*, vol. 41, no. 7, pp. 1046–1053, 2008.

[10] J. Kennewell and B. Vo, "An overview of space situational awareness," in *Proc. Int. Conf. Inf. Fusion*, 2013, pp. 1029–1036.

[11] E. Blasch, M. Pugh, C. Sheaff, J. Raquepas, and P. Rocci, "Big data for space situation awareness," in *Proc. Sensors Syst. Space Appl. X*, 2017, pp. 1–13.

[12] USSTRATCOM, "U.S. Strategic Command Fact Sheet Combined Space Operations Center / 614th Air Operations Center," Jul. 2018. [Online]. Available: https://www.stratcom.mil/Portals/8/Documents/CSpOC_Factsheet_2018.pdf

[13] North American Aerospace Defense Command (NORAD), "Two-line element sets," [Online]. Available: http://celestrak.com/NORAD/elements/

[14] D. Vallado and P. Crawford, "SGP4 orbit determination," in *Proc. AIAA/AAS Astrodynamics Specialist Conf. Exhibit.*, 2008, pp. 6770–6799.

[15] S. Liu et al., "LEO satellite constellations for 5G and beyond: How will they reshape vertical domains?," *IEEE Commun. Mag.*, vol. 59, no. 7, pp. 30–36, Jul. 2021.

[16] T. Reid, K. Gunning, A. Perkins, S. Lo, and T. Walter, "Going back for the future: Large/mega LEO constellations for navigation," in *Proc. ION GNSS Conf.*, 2019, pp. 2452–2468.

[17] B. Li, H. Ge, M. Ge, L. Nie, Y. Shen, and H. Schuh, "LEO enhanced global navigation satellite system (LeGNSS) for real-time precise positioning services," *Adv. Space Res.*, vol. 63, no. 1, pp. 73–93, 2019.

[18] R. Landry, A. Nguyen, H. Rasaee, A. Amrhar, X. Fang, and H. Benzerrouk, "Iridium Next LEO satellites as an alternative PNT in GNSS denied environments—Part 1," *Inside GNSS Mag.*, vol. 14, no. 3, pp. 56–64, May 2019.

[19] S. Thompson, S. Martin, and D. Bevly, "Single differenced Doppler positioning with low Earth orbit signals of opportunity and angle of arrival estimation," in *Proc. ION Int. Tech. Meeting*, 2020, pp. 497–509.

[20] T. Reid et al., "Satellite navigation for the age of autonomy," in *Proc. IEEE/ION Position Location Navigation Symp.*, 2020, pp. 342–352.

[21] J. Khalife, M. Neinavaie, and Z. Kassas, "Navigation with differential carrier phase measurements from megaconstellation LEO satellites," in *Proc. IEEE/ION Position, Location, Navigation Symp.*, 2020, pp. 1393–1404.

[22] Q. Wei, X. Chen, and Y. Zhan, "Exploring implicit pilots for precise estimation of LEO satellite downlink Doppler frequency," *IEEE Commun. Lett.*, vol. 24, no. 10, pp. 2270–2274, Oct. 2020.

[23] F. Farhangian, H. Benzerrouk, and R. Landry, "Opportunistic in-flight INS alignment using LEO satellites and a rotatory IMU platform," *Aerospace*, vol. 8, no. 10, pp. 280–281, 2021.

[24] A. Nardin, F. Dovis, and J. Fraire, "Empowering the tracking performance of LEO-based positioning by means of meta-signals," *IEEE J. Radio Freq. Identif.*, vol. 5, no. 3, pp. 244–253, Sep. 2021.

[25] L. Ye, Y. Yang, X. Jing, L. Deng, and H. Li, "Single-satellite integrated navigation algorithm based on broadband LEO constellation communication links," *Remote Sens.*, vol. 13, no. 4, pp. 703–729, Feb. 2021.

[26] P. Iannucci and T. Humphreys, "Fused low-Earth-orbit GNSS," *IEEE Trans. Aerosp. Electron. Syst.*, to be published, doi: 10.1109/TAES.2022.3180000.

[27] M. Psiaki, "Navigation using carrier Doppler shift from a LEO constellation: TRANSIT on steroids," *NAVIGATION, J. Inst. Navigation*, vol. 68, no. 3, pp. 621–641, Sep. 2021.

[28] Z. Kassas et al., "Enter LEO on the GNSS stage: Navigation with Starlink satellites," *Inside GNSS Mag.*, vol. 16, no. 6, pp. 42–51, 2021.

[29] R. Cassel, D. Scherer, D. Wilburne, J. Hirschauer, and J. Burke, "Impact of improved oscillator stability on LEO-based satellite navigation," in *Proc. ION Int. Tech. Meeting*, 2022, pp. 893–905.

[30] J. Khalife, M. Neinavaie, and Z. Kassas, "The first carrier phase tracking and positioning results with Starlink LEO satellite signals," *IEEE Trans. Aerosp. Electron. Syst.*, vol. 56, no. 2, pp. 1487–1491, Apr. 2022.

[31] S. Kozhaya, J. Haidar-Ahmad, A. Abdallah, Z. Kassas, and S. Saab, "Comparison of neural network architectures for simultaneous tracking and navigation with LEO satellites," in *Proc. ION GNSS Conf.*, 2021, pp. 2507–2520.

[32] N. Khairallah and Z. Kassas, "Ephemeris closed-loop tracking of LEO satellites with pseudorange and Doppler measurements," in *Proc. ION GNSS Conf.*, 2021, pp. 2544–2555.

[33] J. Haidar-Ahmad, N. Khairallah, and Z. Kassas, "A hybrid analytical-machine learning approach for LEO satellite orbit prediction," in *Proc. Int. Conf. Inf. Fusion*, 2022, pp. 1–7.

[34] D. Lawrence et al., "Navigation from LEO: Current capability and future promise," *GPS World Mag.*, vol. 28, no. 7, pp. 42–48, Jul. 2017.

[35] J. Khalife and Z. Kassas, "Receiver design for Doppler positioning with LEO satellites," in *Proc. IEEE Int. Conf. Acoust., Speech, Signal Process.*, 2019, pp. 5506–5510.

[36] F. Farhangian and R. Landry, "Multi-constellation software-defined receiver for Doppler positioning with LEO satellites," *Sensors*, vol. 20, no. 20, pp. 5866–5883, Oct. 2020.

[37] M. Orabi, J. Khalife, and Z. Kassas, "Opportunistic navigation with Doppler measurements from Iridium Next and Orbcomm LEO satellites," in *Proc. IEEE Aerosp. Conf.*, 2021, pp. 1–9.

[38] C. Pinell, "Receiver architectures for positioning with low Earth orbit satellite signals," Master's thesis, School Elect. Eng., Lulea Univ. Technol., Lulea, Sweden, 2021.

[39] C. Zhao, H. Qin, and Z. Li, "Doppler measurements from multiconstellations in opportunistic navigation," *IEEE Trans. Instrum. Meas.*, vol. 71, pp. 1–9, 2022.

[40] M. Neinavaie, J. Khalife, and Z. Kassas, "Cognitive opportunistic navigation in private networks with 5G signals and beyond," *IEEE J. Sel. Topics Signal Process.*, vol. 16, no. 1, pp. 129–143, Jan. 2022.

[41] M. Neinavaie, J. Khalife, and Z. Kassas, "Blind Doppler tracking and beacon detection for opportunistic navigation with LEO satellite signals," in *Proc. IEEE Aerosp. Conf.*, 2021, pp. 1–8.

[42] M. Neinavaie, J. Khalife, and Z. Kassas, "Acquisition, Doppler tracking, and positioning with Starlink LEO satellites: First results," *IEEE Trans. Aerosp. Electron. Syst.*, vol. 58, no. 3, pp. 2606–2610, Jun. 2022.

[43] Z. Kassas, J. Morales, and J. Khalife, "New-age satellite-based navigation–STAN: Simultaneous tracking and navigation with LEO satellite signals," *Inside GNSS Mag.*, vol. 14, no. 4, pp. 56–65, 2019.

[44] N. Khairallah and Z. Kassas, "An interacting multiple model estimator of LEO satellite clocks for improved positioning," in *Proc. IEEE Veh. Technol. Conf.*, 2022, pp. 1–5.

[45] F. Hoots and R. Roehrich, "Spacetrack report no. 3," Dec. 1988. [Online]. Available: http://celestrak.com/NORAD/documentation/spacetrk.pdf

[46] Systems Tool Kit (STK), "High-Precision Orbit Propagator (HPOP)," Sep. 2016. [Online]. Available: https://help.agi.com/stk/11.0.1/Content/hpop/hpop.htm

[47] D. Vallado, "An analysis of state vector propagation using differing flight dynamics programs," in *Proc. AAS Space Flight Mechanics Conf.*, 2005, pp. 1563–1592.

[48] X. Tian, G. Chen, E. Blasch, K. Pham, and Y. Bar-Shalom, "Comparison of three approximate kinematic models for space object tracking," in *Proc. Int. Conf. Inf. Fusion*, 2013, pp. 1005–1012.

[49] M. Hough, "Closed-form nonlinear covariance prediction for two-body orbits," *J. Guid., Control, Dyn.*, vol. 37, no. 1, pp. 26–35, 2014.

[50] K. Vishwajeet, P. Singla, and M. Jah, "Nonlinear uncertainty propagation for perturbed two-body orbits," *J. Guid., Control, Dyn.*, vol. 37, no. 5, pp. 1415–1425, May 2014.

[51] Z. Yang, Y. Luo, V. Lappas, and A. Tsourdos, "Nonlinear analytical uncertainty propagation for relative motion near $j2$-perturbed elliptic orbits," *J. Guid., Control, Dyn.*, vol. 43, no. 4, pp. 888–903, Apr. 2018.

[52] B. Jones and R. Weisman, "Multi-fidelity orbit uncertainty propagation," *Acta Astronautica*, vol. 155, pp. 406–417, 2019.

[53] O. Montenbruck and E. Gill, *Satellite Orbits: Models, Methods, and Applications*. Berlin, Germany: Springer, 2000.

[54] B. Schutz, B. Tapley, and G. Born, *Statistical orbit determination*. Amsterdam, The Netherlands: Elsevier, 2004.

[55] S. Sharma and J. Cutler, "Robust orbit determination and classification: A learning theoretic approach," IPN Progress Rep., vol. 42, no. 203, pp. 1–20, 2015.

[56] B. Lee, W. Kim, J. Lee, and Y. Hwang, "Machine learning approach to initial orbit determination of unknown LEO satellites," in *Proc. AIAA SpaceOps Conf.*, 2018, pp. 1–11.

[57] H. Peng and X. Bai, "Comparative evaluation of three machine learning algorithms on improving orbit prediction accuracy," *Astrodynamics*, vol. 3, no. 4, pp. 325–343, 2019.

[58] H. Peng and X. Bai, "Machine learning approach to improve satellite orbit prediction accuracy using publicly available data," *J. Astronautical Sci.*, vol. 67, no. 2, pp. 762–793, 2020.

[59] B. Li, J. Huang, Y. Feng, F. Wang, and J. Sang, "A machine learning-based approach for improved orbit predictions of LEO space debris with sparse tracking data from a single station," *IEEE Trans. Aerosp. Electron. Syst.*, vol. 56, no. 6, pp. 4253–4268, Dec. 2020.

[60] T. Mortlock and Z. Kassas, "Assessing machine learning for LEO satellite orbit determination in simultaneous tracking and navigation," in *Proc. IEEE Aerosp. Conf.*, 2021, pp. 1–8.

[61] J. Vetter, "Fifty years of orbit determination: Development of modern astrodynamics methods," *Johns Hopkins APL Tech. Dig.*, vol. 27, no. 3, pp. 239–252, Nov. 2007.

[62] B. Tapley et al., "The joint gravity model 3," *J. Geophysical Res.*, vol. 101, no. B12, pp. 28029–28049, Dec. 1996.

[63] J. Vinti, *Orbital and Celestial Mechanics*. Reston, VA, USA: Amer. Inst. Aeronautics Astronaut., 1998.

[64] R. Brown and P. Hwang, *Introduction to Random Signals and Applied Kalman Filtering With Matlab Exercises*, 4th ed. Hoboken, NJ, USA: Wiley, 2012.

[65] A. Thompson, J. Moran, and G. Swenson, *Interferometry and Synthesis in Radio Astronomy*, 2nd ed. Hoboken, NJ, USA: Wiley, 2001.

[66] P. Misra and P. Enge, *Global Positioning System: Signals, Measurements, and Performance*, 2nd ed. Philadelphia, PA, USA: Ganga-Jamuna Press, 2010.

[67] R. Sabbagh and Z. Kassas, "Observability analysis of receiver localization via pseudorange measurements from a single LEO satellite," *IEEE Control Syst. Lett.*, vol. 7, no. 3, pp. 571–576, 2023.

[68] M. Kenny, "Ever wondered what is on the Orbcomm satellite downlink?," 2002. [Online]. Available: http://mdkenny.customer. netspace.net.au/Orbcomm.pdf

[69] D. Vallado, P. Crawford, R. Hujsak, and T. Kelso, "Revisiting space-track report# 3," in *Proc. Astrodynamics Specialist Conf. Exhibit.*, 2006, no. 6753, pp. 1–88.

[70] J. Morales, J. Khalife, U. S. Cruz, and Z. Kassas, "Orbit modeling for simultaneous tracking and navigation using LEO satellite signals," in *Proc. ION GNSS Conf.*, 2019, pp. 2090–2099.

Zaher (Zak) M. Kassas (Fellow, IEEE) received the B.E. degree in electrical engineering from the Lebanese American University, Beirut, Lebanon, the M.S. degree in electrical and computer engineering from The Ohio State University, Columbus, OH, USA, and the M.S.E. degree in aerospace engineering and the Ph.D. degree in electrical and computer engineering from The University of Texas at Austin, Austin, TX, USA.

He is currently a Professor with The Ohio State University, Columbus, OH, USA, and the TRC Endowed Chair in intelligent transportation systems. He is the Director of the Autonomous Systems Perception, Intelligence, and Navigation (ASPIN) Laboratory, University of California, Irvine, CA, USA. He is also the Director of the U.S. Department of Transportation Center: Center for Automated Vehicle Research With Multimodal Assured Navigation, focusing on navigation resiliency and security of highly automated transportation systems. His research interests include cyber-physical systems, navigation systems, and intelligent transportation systems.

Dr. Kassas is a recipient of the National Science Foundation (NSF) CAREER award, Office of Naval Research (ONR) Young Investigator Program (YIP) award, Air Force Office of Scientific Research (AFOSR) YIP award, IEEE Walter Fried Award, Institute of Navigation (ION) Samuel Burka Award, and ION Col. Thomas Thurlow Award. He is an Associate Editor for IEEE TRANSACTIONS ON AEROSPACE AND ELECTRONIC SYSTEMS and a Senior Editor for IEEE TRANSACTIONS ON INTELLIGENT TRANSPORTATION SYSTEMS. He is a Fellow of the IEEE, a Fellow of the ION, and a Distinguished Lecturer of the IEEE Aerospace and Electronic Systems Society.

Nadim Khairallah received the B.E. degree in mechanical engineering with High Distinction from the American University of Beirut, Beirut, Lebanon, and the M.S. degree in mechanical and aerospace engineering from the University of California, Irvine, Irvine, CA, USA.

He was a member of Autonomous Systems Perception, Intelligence, and Navigation (ASPIN) Laboratory. His research interests include satellite-based opportunistic navigation, sensor fusion, and estimation theory.

Mr. Khairallah is a recipient of the 2021 US Department of Transportation Graduate Student of the Year award and the 2022 IEEE Vehicular Technology Conference best student paper award.